Comparative Analysis of Subgrid Drag Modifications for Dense Gas-Particle Flows in Bubbling Fluidized Beds

Simon Schneiderbauer, Stefan Puttinger, and Stefan Pirker
Christian-Doppler Laboratory for Particulate Flow Modelling, Johannes Kepler University, Altenbergerstr. 69,
Linz, Austria

Dept. of Particulate Flow Modelling, Johannes Kepler University, Altenbergerstr. 69, Linz, Austria

DOI 10.1002/aic.14155

Many subgrid drag modifications have been put forth to account for the effect of small unresolved scales on the resolved mesoscales in dense gas-particle flows. These subgrid drag modifications significantly differ in terms of their dependencies on the void fraction and the particle slip velocity. We, therefore, compare the hydrodynamics of a three-dimensional bubbling fluidized bed computed on a coarse grid using the drag correlations of the groups of (i) EMMS, (ii) Kuipers, (iii) Sundaresan, (iv) Simonin, and the homogenous drag law of (v) Wen and Yu with fine grid simulations for two different superficial gas velocities. Furthermore, we present an (vi) alternative approach, which distinguishes between resolved and unresolved particle clusters revealing a grid and slip velocity dependent heterogeneity index. Numerical results are analyzed with respect to the time-averaged solids volume fraction and its standard deviation, gas and solid flow patterns, bubble size, number density, and rise velocities. © 2013 American Institute of Chemical Engineers *AIChE J*, 59: 4077–4099, 2013

Keywords: bubbling fluidized beds, subgrid drag modifications, kinetic-theory based TFM, coarse-grid simulations, computational fluid dynamics

Introduction

Fluidized beds are widely used in process industries, for example, for biomass reactors,[1–4] polymerization reactors,[5–7] and combustion.[8] The favorable properties of fluidized beds, that is, a high degree of particle mixing and the effective particle-fluid heat transfer, have been known even since the 1940s of the 20th century.[9–11] The investigation of these was, however, restricted to simple experimental techniques and analytical considerations. In the past decades, increasing computer power has become available and the numerical simulation of fluidized beds has become feasible opening a third branch to investigate bubbling fluidized beds[12–18] and spout beds.[19–25]

Due to computational limitations, a highly resolved simulation of industrial scale reactors is still unfeasible.[26–33] It is, therefore, common to use coarse grids to reduce the demand on computational resources. However, such a procedure inevitably neglects small (unresolved) scales, which leads to a considerable overestimation of the bed expansion in the case of fine particles.[28,34–37] It is generally agreed that the influence of these small scales on the drag force is a key parameter in the prediction of the bed expansion (Ref. 28 and references cited therein). Many subgrid drag modifications have, therefore, been put forth by academic researchers to account for the effect of small unresolved scales on the resolved mesoscales in this case.[26–28,38–42]

In the case of two-fluid models (TFM), in recent years several authors[43–46] studied the effect of the unresolved mesoscale scales on the macroscale momentum equations. Especially, the drag force is overestimated if these small scales are not resolved by the mesh.[38,45,46] This, in turn, implies that the numerical simulation of fluidized bed reveals a considerable mesh dependence. Andrews et al.[47] suggested that a grid-independent solution could be obtained using a grid size with less than 10 particle diameters, which was also supported by other studies.[30–33] More recently, several authors studied the impact of the effective subgrid stresses on coarse meshes by filtering fine grid simulations.[38,39,48,49] Although, it appears that the bed expansion is nearly independent of the unresolved contribution of the particle stresses and the magnitude of the drag force is much larger than the particle stresses,[28] neglecting their unresolved contribution produces quantitative changes in the predicted results.[39] Thus, in the case of industrial scale fluidized beds, additional closures for the unresolved small scales become indispensable[30–32] and an adequate modeling of the unresolved part of the drag is essential to predict the correct bed expansion.[28]

In recent years, several approaches have been proposed to account for the effect of these unresolved scales on the drag correlation, when applying TFMs to coarse meshes. The EMMS model[50–52] was one of the first approaches dealing with the influence of heterogenous structures on the drag

---

Correspondence concerning this article should be addressed to Simon Schneiderbauer at simon.schneiderbauer@jku.at.

force. It is assumed that these structures appear as distinct-particle clusters within an interstitial dilute particle phase, where both require additional modeling. The clusters and the dilute phase consist themselves of homogeneously distributed particles, enabling the application of a homogenous drag correlation to these structures. The resulting underdetermined set of equations is solved by minimizing the energy consumed by the transport of the particles, referred to as stability condition. More recently, derivates of the EMMS model have been proposed to account for transient flows (EMMS/matrix model[26,53–57]), the gas-phase pressure gradient (cluster structure-dependent drag coefficient[40,41]), and bubbling fluidized beds.[58] The groups of Simonin[28,59] and Sundaresan[38,39] derived residual correlations from filtering highly resolved simulations. The results of Parmentier et al.[28] suggest that the overestimation of the drag force is linked to the existence of a subgrid drift velocity, which reduces the effective resolved slip velocity. In contrast to the EMMS model, both approaches reveal a significant dependence of the effective drag on the filter length and, therefore, on the mesh size. However, while the drag modification of the group of Simonin has solely been tuned and tested for a specific case, the correlation of the group of Sundaresan has already been verified for more general gas-particle flows in risers.[29,60] Wang et al.[27] proposed a modification of homogenous drag models to account for heterogenous structures in bubbling fluidized beds. By neglecting the drag force on the particles in the bubble phase and by applying empirical correlations to the solids volume fraction in the dense phase, the volume fraction of the bubbles can be determined. Thus, the drag exerted on the dense phase can be computed yielding fairly good agreement with measurements of Werther and Wein[61] with respect to the bed expansion. Another drag modification for bubbling fluidized beds has been proposed by Schneiderbauer et al.,[42] which can be regarded as considerable simplification of the EMMS model. By ignoring the drag on the particles in the dilute phase, the underlying EMMS balance equations[26,53,54] can be solved rendering an additional stability condition unnecessary. Furthermore, in contrast to EMMS and its derivatives, the model of Schneiderbauer et al.[42] distinguishes between resolved and unresolved clusters by computing the expectation value of the diameter of the unresolved clusters. This, in turn, implies that the drag modification recovers the homogenous drag law as the solids volume fraction approaches the maximum packing of frictional spheres. Finally, other researchers[62,63] suggest a completely different approach. Bubbles may be modeled as discrete elements, which can be tracked individually during their rise through the emulsion phase. Such an approach simplifies the hydrodynamics of a bubbling fluidized bed to a single-phase problem but requires additional assumptions about closure relations for the bubble behavior.

However, the general applicability of previously mentioned modifications of homogenous drag correlations to bubbling fluidized beds is still unverified. For example, the EMMS model was originally developed for risers using Geldart A particles. The highly resolved simulations of Igci et al.[39] consider the contribution from the frictional solids stresses in regions only, where the solids volume fraction exceeds 0.59. In this regime, also spare resolved data were available to derive the residual correlations for the effective drag.[39] However, frictional stresses may become important even at significantly smaller solids volume fractions.[23,64–67] Parmentier et al.[28] introduced a parameter, which was dynamically adjusted by a second filter operation following a methodology proposed by Germano et al.,[68] and Lilly.[69] Thus, this parameter may depend strongly on the simulation case and the grid resolution. Finally, comparative studies of these subgrid drag modifications appear incomplete. For example, in the study of Benyahia[70], only a simplified version of EMMS[71] for relatively dilute flow conditions and the filtered drag of Igci et al.[38] are applied to the gas-particle flow of Geldart type A particles in a riser.

This article focuses on a comparative analysis of state-of-the-art TFM subgrid modifications of the drag law for dense gas-particle flows. First, we discuss the requirements of subgrid modeling with respect to the governing equations of TFMs. Second, the modifications of EMMS,[26] Wang et al.,[27] Igci et al.,[39] and Parmentier et al.[28] are analyzed in detail. Then, following Schneiderbauer et al.,[42] we present an effective drag correlation for TFMs accounting for unresolved scales, that is, subgrid structures in bubbling fluidized beds. For the presentation of the different models, we lay special attention on a consistent notation. A detailed comparison of the different modifications reveals a significant difference of the functional dependencies on the void fraction and the slip velocity. Next, these drag correlations are applied to a bubbling fluidized bed of fine glass particles (Geldart type B) for two different inflow gas velocities. As there is no fundamental difference between the numerical modeling of gas-particle flows of Geldart A and Geldart B particles,[30] we also consider subgrid drag modifications developed originally for Geldart type A particles. The numerical results are analyzed with respect to the bed expansion, time averaged solids volume fraction profiles with their corresponding standard deviations, time-averaged superficial gas flow, time-averaged particle mass fluxes, and bubble properties including bubble size, bubble number density, and bubble rise velocities. A conclusion ends this article.

Subgrid Drag Models

In general, the TFM equations given in the appendix (Table 3) are derived by translating the Newton's equation of motion for a single particle directly into continuum equations representing the momentum balances for the solid phase.[15,72–74] To obtain equations for continuous space-time variables, $g(\boldsymbol{x},t)$, the point variables, $\widehat{g}(\boldsymbol{x},t)$, are averaged by introducing a weighting function G_l, which is normalized to unity

$$\iiint G_l(||\boldsymbol{x}-\boldsymbol{y}||)dV_{\boldsymbol{y}}=1$$

$\boldsymbol{x}-\boldsymbol{y}$ denotes the distance vector between two points in space, $\boldsymbol{x}$ and $\boldsymbol{y}$, and $dV_{\boldsymbol{y}}$ indicates the volume integration with respect to $\boldsymbol{y}$. l is the "radius" of G_l, which is in spherical coordinates determined by[15]

$$\int_0^l G_l(r)r^2dr=\int_l^\infty G_l(r)r^2dr$$

Thus, $g(\boldsymbol{x},t)$ is given by

$$g(\boldsymbol{x},t)=\iiint G_l(||\boldsymbol{x}-\boldsymbol{y}||)\widehat{g}(\boldsymbol{y},t)dV_{\boldsymbol{y}} \tag{1}$$

The above procedure requires that the averaging region, that is, l, is large with respect to the particle diameter and

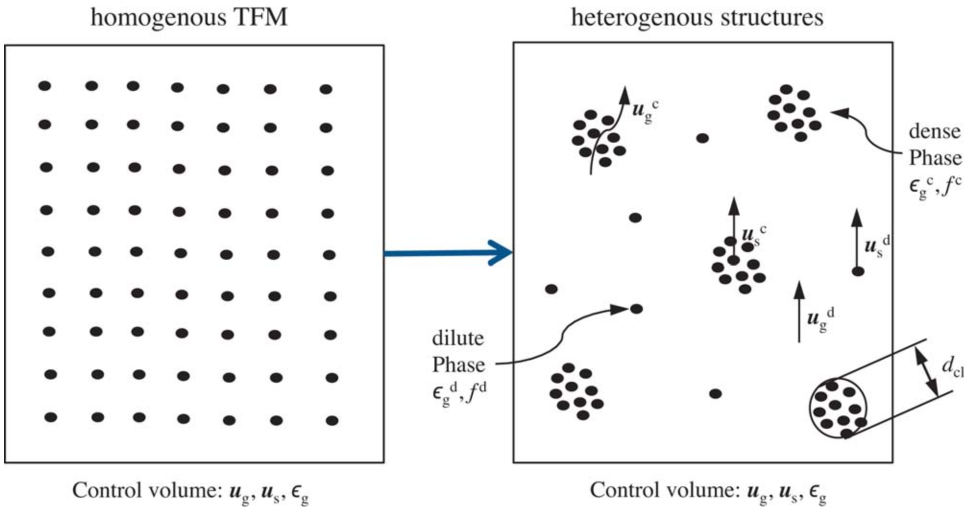

Figure 1. The schematic diagram of the subgrid heterogeneity.[26,42,57]

[Color figure can be viewed in the online issue, which is available at wileyonlinelibrary.com.]

small with respect to the characteristic dimension of the system.[15] In addition, the gas and solids volume fractions of monodispersed grains are directly connected to G_l yielding

$$\epsilon_g(\boldsymbol{x},t)=\iiint_{V_g(t)} G_l(||\boldsymbol{x}-\boldsymbol{y}||)dV_{\boldsymbol{y}}$$

$$\epsilon_s(\boldsymbol{x},t)=V_p\sum_p G_l\Big(||\boldsymbol{x}-\boldsymbol{y}_p(t)||\Big)$$

where V_g denotes the volume of the gas phase, V_p the volume of a single particle, and $\boldsymbol{y}_p$ the position of the center of particle p. By applying the above averaging rules to the point continuity and momentum equations of the fluid and to the equation of motion of a single particle one obtains Eqs. 54–56. Wang et al.[30] suggested that from a modeling point of view Geldart A and Geldart B particles can be treated similarly by kinetic theory-based TFM.[75–77] In the case of Geldart B particles, these are reported to successfully predict the hydrodynamics of bubbling fluidized beds, especially, the bed expansion and the bubble dynamics.[15,78,79]

It is common to solve the resulting TFM equations by discretizing these equations in time and space. The latter yields corresponding equations for the spatially resolved parts of the transport variables, whereas the unresolved parts are omitted. Balance laws for these unresolved parts can be found from a second filtering operation of the continuous space-time variables $g(\boldsymbol{y},t)$ yielding the filtered part of $g(\boldsymbol{y},t)$ and, therefore, the discretized or resolved part[28,38,45,46]

$$\overline{g}(\boldsymbol{x},t)=\iiint G_\Delta(||\boldsymbol{x}-\boldsymbol{y}||)g(\boldsymbol{y},t)dV_{\boldsymbol{y}} \tag{2}$$

with the weighting function $G_\Delta(||\boldsymbol{x}-\boldsymbol{y}||)$ also satisfying $\iiint G_\Delta(||\boldsymbol{x}-\boldsymbol{y}||)dV_{\boldsymbol{y}}=1$. The subscript Δ indicates that $l_\Delta \gtrsim \Delta$, where Δ is the grid spacing and l_Δ the "radius" of G_Δ. By applying Eq. 2 to the momentum equations (Eqs. 55 and 56 listed in Table 3 in the appendix) additional terms representing the unresolved contributions arise. Equation 2 implies that in the case of $l \gtrsim l_\Delta (\gtrsim \Delta)$ the unresolved parts of continuous variables vanish and, therefore, with respect to l the resolved results can be obtained. In the literature, it is generally agreed that Δ should be equal or less than $10d_s$ in the case of Geldart A and B particles,[30–33,47] requiring closure models for the unresolved parts on coarse grids. The results of Parmentier et al.[28] suggest that in the first place the unresolved part of the drag has to be modeled adequately to predict the correct bed expansion of bubbling and turbulent fluidized beds. It has to be noted that although the magnitude of the drag force is much larger than the particle stresses, neglecting their unresolved contribution produces quantitative changes in the predicted results.[39] However, in this study, we focus on the impact of drag modifications only. Commonly, the effective filtered drag force is modeled by a multiplicative approach[26,28,38,50,57]

$$\overline{\beta(\boldsymbol{u}_g-\boldsymbol{u}_s)}=H_d\overline{\beta}(\overline{\boldsymbol{u}}_g-\overline{\boldsymbol{u}}_s) \tag{3}$$

where $\overline{\beta}$ denotes the homogenous drag correlation computed from filtered (resolved) variables, and H_d is a function accounting for the unresolved structures. According to van Wachem et al.,[15] the drag correlation of Wen and Yu[80] (Eq. 58) is adequate in the case of bubbling fluidized beds and, thus, we set $\overline{\beta}=\overline{\beta}_{WY}$. According to the EMMS group, H_d is referred to as heterogeneity index. In order to comply Eq. 2, a closure for H_d should approach unity for sufficiently small grid spacing. Note that we skip the overbars indicating filtered variables in the following discussion for better readability.

EMMS

The EMMS model was originally presented by Li and Kwauk[50] and is based on the assumption that the heterogeneity inside fluidized beds, especially risers, is caused by the formation of local clusters, which is also supported by experiments.[81–87] Inside (dense phase) and outside (dilute phase) a cluster, the particles are considered to be homogeneously distributed (Figure 1). In the case of fast fluidization of Geldart A particles in risers, the EMMS model is reported to capture experimental data successfully.[26,52,55,71,88–94]

The above decomposition of the homogenous system into particles inside and outside of clusters (Figure 1) yields a set of constraint conditions. In the first place, the pressure balance between clusters and dilute phase reads[26,54,57]

$$\boldsymbol{F}^{\mathrm{d}}_{\mathrm{d}} + \frac{1}{f^{\mathrm{d}}}\boldsymbol{F}^{\mathrm{cl}}_{\mathrm{d}} = \boldsymbol{F}^{\mathrm{c}}_{\mathrm{d}} \tag{4}$$

with

$$\begin{aligned}
\boldsymbol{F}^{\mathrm{d}}_{\mathrm{d}} &= \frac{3}{4} C^{\mathrm{d}}_{\mathrm{d}} \frac{\rho_{\mathrm{g}}\epsilon^{\mathrm{d}}_{\mathrm{g}}\epsilon^{\mathrm{d}}_{\mathrm{s}}}{d_{\mathrm{s}}} ||\boldsymbol{u}^{\mathrm{d}}_{\mathrm{g}} - \boldsymbol{u}^{\mathrm{d}}_{\mathrm{s}}|| \left(\boldsymbol{u}^{\mathrm{d}}_{\mathrm{g}} - \boldsymbol{u}^{\mathrm{d}}_{\mathrm{s}}\right) \\
\boldsymbol{F}^{\mathrm{cl}}_{\mathrm{d}} &= \frac{3}{4} C^{\mathrm{cl}}_{\mathrm{d}} \frac{\rho_{\mathrm{g}}\epsilon_{\mathrm{g}}\epsilon_{\mathrm{s}}}{d_{\mathrm{cl}}} ||\boldsymbol{u}^{\mathrm{d}}_{\mathrm{g}} - \boldsymbol{u}^{\mathrm{c}}_{\mathrm{s}}|| \left(\boldsymbol{u}^{\mathrm{d}}_{\mathrm{g}} - \boldsymbol{u}^{\mathrm{c}}_{\mathrm{s}}\right) \\
\boldsymbol{F}^{\mathrm{c}}_{\mathrm{d}} &= \frac{3}{4} C^{\mathrm{c}}_{\mathrm{d}} \frac{\rho_{\mathrm{g}}\epsilon^{\mathrm{c}}_{\mathrm{g}}\epsilon^{\mathrm{c}}_{\mathrm{s}}}{d_{\mathrm{s}}} ||\boldsymbol{u}^{\mathrm{c}}_{\mathrm{g}} - \boldsymbol{u}^{\mathrm{c}}_{\mathrm{s}}|| \left(\boldsymbol{u}^{\mathrm{c}}_{\mathrm{g}} - \boldsymbol{u}^{\mathrm{c}}_{\mathrm{s}}\right)
\end{aligned} \tag{5}$$

$\boldsymbol{F}^{\mathrm{d}}_{\mathrm{d}}$ denotes the drag force per unit volume on the particles in the dilute phase and $\boldsymbol{F}^{\mathrm{c}}_{\mathrm{d}}$ is the drag force on the particles in the dense phase. The drag force $\boldsymbol{F}^{\mathrm{cl}}_{\mathrm{d}}$ arises from the interaction between the surrounding dilute-phase gas and the particle clusters. The superscripts d, c, and cl, therefore, refer to the dilute phase, the dense phase inside particle clusters, and the particle clusters of diameter d_{cl} (see also Figure 1). As the particles and clusters are homogeneously distributed, the drag coefficients for particles in the dilute phase, $C^{\mathrm{d}}_{\mathrm{d}}$, for particles in the dense phase (cluster), $C^{\mathrm{c}}_{\mathrm{d}}$, and for the clusters, $C^{\mathrm{cl}}_{\mathrm{d}}$, can be closed by, for example, using the homogenous drag coefficient of Wen and Yu[80]

$$C^{i}_{\mathrm{d}} = \frac{24}{\mathrm{Re}^{i}_{\mathrm{s}}}\left(1 + 0.15\left(\mathrm{Re}^{i}_{\mathrm{s}}\right)^{0.687}\right)\left(\epsilon^{i}_{\mathrm{g}}\right)^{-2.65} \tag{6}$$

$$C^{\mathrm{cl}}_{\mathrm{d}} = \frac{24}{\mathrm{Re}^{\mathrm{cl}}_{\mathrm{s}}}\left(1 + 0.15\left(\mathrm{Re}^{\mathrm{cl}}_{\mathrm{s}}\right)^{0.687}\right)\epsilon_{\mathrm{g}}^{-2.65} \tag{7}$$

with the Reynolds numbers

$$\mathrm{Re}^{i}_{\mathrm{s}} = \frac{\epsilon^{i}_{\mathrm{g}}\rho_{\mathrm{g}}||\boldsymbol{u}^{i}_{\mathrm{g}} - \boldsymbol{u}^{i}_{\mathrm{s}}||d_{\mathrm{s}}}{\mu_{\mathrm{g}}}, \quad \mathrm{Re}^{\mathrm{cl}}_{\mathrm{s}} = \frac{\epsilon_{\mathrm{g}}\rho_{\mathrm{g}}||\boldsymbol{u}^{\mathrm{d}}_{\mathrm{g}} - \boldsymbol{u}^{\mathrm{c}}_{\mathrm{s}}||d_{\mathrm{cl}}}{\mu_{\mathrm{g}}}$$

where $i \in \{\mathrm{d}, \mathrm{c}\}$. f^{c} denotes the volume fraction of the particle clusters, which is connected to the volume fraction of the dilute phase as follows

$$f^{\mathrm{d}} = 1 - f^{\mathrm{c}} \tag{8}$$

The effective drag coefficient, β_{E}, accounting for the heterogeneity can be derived from Eq. 5 yielding

$$\beta_{\mathrm{E}} = \frac{1}{||\boldsymbol{u}_{\mathrm{g}} - \boldsymbol{u}_{\mathrm{s}}||}||f^{\mathrm{d}}\boldsymbol{F}^{\mathrm{d}}_{\mathrm{d}} + \boldsymbol{F}^{\mathrm{cl}}_{\mathrm{d}} + f^{\mathrm{c}}\boldsymbol{F}^{\mathrm{c}}_{\mathrm{d}}|| \tag{9}$$

Note that Eq. 9 is compatible with Eqs. 55 and 56. According to Eq. 9, H_{d} equals $\beta_{\mathrm{E}}/\beta_{\mathrm{WY}}$ in our study and thus, the effective drag coefficient reads

$$\beta = \beta_{\mathrm{E}} \tag{10}$$

Additionally, $\boldsymbol{u}^{i}_{\mathrm{g}}$ and $\boldsymbol{u}^{i}_{\mathrm{s}}$ ($i \in \{\mathrm{d}, \mathrm{c}\}$) satisfy the mass conservation for the fluid[54,57]

$$\epsilon_{\mathrm{g}}\boldsymbol{u}_{\mathrm{g}} = \epsilon^{\mathrm{d}}_{\mathrm{g}}\boldsymbol{u}^{\mathrm{d}}_{\mathrm{g}}f^{\mathrm{d}} + \epsilon^{\mathrm{c}}_{\mathrm{g}}\boldsymbol{u}^{\mathrm{c}}_{\mathrm{g}}f^{\mathrm{c}} \tag{11}$$

and for the particle phase

$$\epsilon_{\mathrm{s}}\boldsymbol{u}_{\mathrm{s}} = \epsilon^{\mathrm{d}}_{\mathrm{s}}\boldsymbol{u}^{\mathrm{d}}_{\mathrm{s}}f^{\mathrm{d}} + \epsilon^{\mathrm{c}}_{\mathrm{s}}\boldsymbol{u}^{\mathrm{c}}_{\mathrm{s}}f^{\mathrm{c}} \tag{12}$$

Furthermore, the mean voidage ϵ_{g} is given by

$$\epsilon_{\mathrm{g}} = \epsilon^{\mathrm{d}}_{\mathrm{g}}f^{\mathrm{d}} + \epsilon^{\mathrm{c}}_{\mathrm{g}}f^{\mathrm{c}} \tag{13}$$

Note that the set of balance Eqs. 4, 11–13 does not account for the drag between dilute phase particles and clusters. Obviously, this set of equations (10 equations) is not closed and, thus, β_{E} can not be computed from Eq. 9. In detail, we have 18 unknowns, these are $\boldsymbol{u}^{i}_{\mathrm{g}}$, $\boldsymbol{u}^{i}_{\mathrm{s}}$, $\epsilon^{i}_{\mathrm{g}}$, $\epsilon^{i}_{\mathrm{s}}$, f^{c}, and d_{cl}, which can be reduced to 16 by using $\epsilon^{i}_{\mathrm{s}} = 1 - \epsilon^{i}_{\mathrm{g}}$. In the current versions of EMMS, experimental correlations are used to compute d_{cl} and $\epsilon^{\mathrm{c}}_{\mathrm{g}}$, but the system of equations is still not closed. Thus, a cost function N_{st}, which describes the energy consumed by the suspension and the transport of particles, is minimized to close the set of equations.[54] Li and Kwauk[50] proposed that N_{st} can be written as

$$N_{\mathrm{st}} = \frac{1}{\left(1 - \epsilon_{\mathrm{g}}\right)\rho_{\mathrm{s}}}\left(f^{\mathrm{d}}\epsilon^{\mathrm{d}}_{\mathrm{g}}\left(\boldsymbol{F}^{\mathrm{cl}}_{\mathrm{d}} \cdot \boldsymbol{u}^{\mathrm{d}}_{\mathrm{g}}\right) + \sum_{i \in \{c,d\}} f^{i}\epsilon^{i}_{\mathrm{g}}\left(\boldsymbol{F}^{i}_{\mathrm{d}} \cdot \boldsymbol{u}^{i}_{\mathrm{g}}\right)\right) \rightarrow \min \tag{14}$$

However, computing β_{E} during a coarse grid simulation is very inefficient because a nonlinear optimization problem (14) has to be solved. It is, therefore, common to correlate the solution of the optimization problem with functions of the Reynolds number, Re, and the mean voidage, ϵ_{g}. For example, the EMMS version of Lu et al.[26] can be fitted by the function $H_{\mathrm{d}} = a(\mathrm{Re} + b)^{c}$, where the coefficients a, b, and c are functions of ϵ_{g}. These are summarized in Table 1.

Drag Model of Kuipers' Group

In the case of bubbling and slugging fluidized beds of Geldart type B particles, the solids volume fraction within bubbles is very low. The drag force exerted on these particles may, therefore, be negligible compared to the drag exerted on the particles in the dense phase. Thus, the drag force is[27]

$$\boldsymbol{F}_{\mathrm{K}} = f^{\mathrm{de}}\beta_{\mathrm{WY}}\left(\epsilon^{\mathrm{de}}_{\mathrm{g}}, \mathrm{Re}^{\mathrm{de}}_{\mathrm{s}}\right)\boldsymbol{u}^{\mathrm{de}}_{\mathrm{sg}} \tag{15}$$

where $\epsilon^{\mathrm{de}}_{\mathrm{g}}$ and $\boldsymbol{u}^{\mathrm{de}}_{\mathrm{sg}}$ denote the voidage and the gas velocity in the dense phase. f^{de} indicates that only a part of a computational cell is occupied by the dense phase. The particle Reynolds number in the dense phase, $\mathrm{Re}^{\mathrm{de}}_{\mathrm{s}}$, is given by

$$\mathrm{Re}^{\mathrm{de}}_{\mathrm{s}} = \frac{\epsilon^{\mathrm{de}}_{\mathrm{g}}\rho_{\mathrm{g}}d_{\mathrm{s}}u^{\mathrm{de}}_{\mathrm{gs}}}{\mu_{\mathrm{g}}}$$

As the solids volume fraction in the bubble phase is assumed to vanish, that is, $\epsilon_{\mathrm{g}} = \left(1 - f^{\mathrm{de}}\right) + f^{\mathrm{de}}\epsilon^{\mathrm{de}}_{\mathrm{g}}$, the final drag coefficient reads

$$\beta_{\mathrm{K}} = \beta_{\mathrm{WY}}\left(\epsilon^{\mathrm{de}}_{\mathrm{g}}, \mathrm{Re}^{\mathrm{de}}_{\mathrm{s}}\right)\frac{\epsilon_{\mathrm{s}}}{\epsilon^{\mathrm{de}}_{\mathrm{s}}}\frac{u^{\mathrm{de}}_{\mathrm{sg}}}{||\boldsymbol{u}_{\mathrm{g}} - \boldsymbol{u}_{\mathrm{s}}||} \tag{16}$$

However, neither $\epsilon^{\mathrm{de}}_{g}$ ($\epsilon^{\mathrm{de}}_{\mathrm{s}} = 1 - \epsilon^{\mathrm{de}}_{\mathrm{g}}$) nor $u^{\mathrm{de}}_{\mathrm{sg}}$ are known *a priori*. Thus, experimental correlations are used to close (16). $\epsilon^{\mathrm{de}}_{\mathrm{g}}$ is calculated from[61]

$$\frac{\epsilon^{\mathrm{de}}_{\mathrm{s}}}{\epsilon^{\mathrm{mf}}_{\mathrm{s}}} = 1 - 0.14\mathrm{Re}_{\mathrm{W}}^{0.4}\mathrm{Ar}_{\mathrm{W}}^{-0.13} \tag{17}$$

with

Table 1. Fitting Formulae for Regressed Heterogeneity Index, H_d, of the Form $H_d=a(\mathrm{Re}+b)^c$ for EMMS Model[26]

$a=0.8526-\frac{0.5846}{1+\left(\in_g/0.4325\right)^{22.6279}} a=0.85$ $c=0$	$0.4 \le \in_g \le 0.46$
$a=0.0320+\frac{0.7399}{1+\left(\epsilon_g/0.4912\right)^{54.4265}}$ $b=0.00225+\frac{772.0074}{1+10^{66.3224\left(\epsilon_g-0.3987\right)}}+\frac{0.02404}{1+10^{53.8948\left(0.5257-\epsilon_g\right)}}$ $c=0.1705-\frac{0.1731}{1+\left(\epsilon_g/0.5020\right)^{37.7091}}$	$0.46 \le \epsilon_g \le 0.545$
$a=\left(2124.956-2142.349\epsilon_g\right)^{-0.4896}$ $b=\left(0.8223-0.1293\epsilon_g\right)^{13.0310}$ $c=\frac{\epsilon_g-1.0013}{-0.06633+9.1391\left(\epsilon_g-1.0013\right)+6.9231\left(\epsilon_g-1.0013\right)^2}$	$0.545 \le \epsilon_g \le 0.99$
$a=0.4243+\frac{0.88}{1+\exp\left(-\left(\epsilon_g-0.9942\right)/0.00218\right)}\left(1-\frac{1}{1+\exp\left(-\left(\epsilon_g-0.9989\right)/0.00003\right)}\right)$ $b=0.01661+0.246\exp\left[-0.5\left(\frac{\epsilon_g-0.9985}{0.00191}\right)^2\right]$ $c=0.0825-0.0574\exp\left[-0.5\left(\frac{\epsilon_g-0.9979}{0.00703}\right)^2\right]$	$0.99 \le \epsilon_g \le 0.9997$
$a=1,\ c=0$	$0.9997 \le \epsilon_g \le 1$

The values of a, b, and c are valid for a Reynolds number range of $0.001 \le \mathrm{Re} \le 35$.

$$Re_{\mathrm{W}}=\frac{\rho_{\mathrm{g}} d_{\mathrm{s}}\|\epsilon_{\mathrm{g}}\|\boldsymbol{u}_{\mathrm{g}}-\boldsymbol{u}_{\mathrm{s}}\|-\epsilon_{\mathrm{g}}^{\mathrm{mf}}u_{\mathrm{g}}^{\mathrm{mf}}\|}{\mu_{\mathrm{g}}}$$

$$\mathrm{Ar}_{\mathrm{W}}=\frac{\rho_{\mathrm{g}} d_{\mathrm{s}}^3\left(\rho_{\mathrm{s}}-\rho_{\mathrm{g}}\right)g}{\mu_{\mathrm{g}}^2}$$

Here, $u_{\mathrm{g}}^{\mathrm{mf}}$ denotes the gas velocity, $\epsilon_{\mathrm{g}}^{\mathrm{mf}}$ ($\epsilon_{\mathrm{s}}^{\mathrm{mf}}$) the voidage (solids volume fraction) at minimum fluidization conditions, and g the standard acceleration due to gravity. Finally, $u_{\mathrm{sg}}^{\mathrm{de}}$ can be calculated from[95]

$$\frac{\epsilon_{\mathrm{g}}^{\mathrm{de}}u_{\mathrm{sg}}^{\mathrm{de}}}{u_{\mathrm{t}}}=\left(\epsilon_{\mathrm{g}}^{\mathrm{de}}\right)^n \tag{18}$$

where u_{t} is the terminal settling velocity of a single particle. The exponent n is given by[96]

$$n=\frac{\ln(\epsilon_{\mathrm{g}}^{\mathrm{mf}}\boldsymbol{u}_{\mathrm{g}}^{\mathrm{mf}}/\boldsymbol{u}_{\mathrm{t}})}{\ln(\epsilon_{\mathrm{g}}^{\mathrm{mf}})}$$

It has to be noted that in the numerical simulation β_{K} is set to β_{WY} when the voidage is less than $\epsilon_{\mathrm{g}}^{\mathrm{mf}}$ or $\epsilon_{\mathrm{g}}\|\boldsymbol{u}_{\mathrm{g}}-\boldsymbol{u}_{\mathrm{s}}\|$ is less than $\epsilon_{\mathrm{g}}^{\mathrm{mf}}u_{\mathrm{g}}^{\mathrm{mf}}$.

Drag Model of Princeton Group

Igci et al.[38] and Igci and Sundaresan[60] presented a methodology, where highly resolved TFM simulations of the gas-particle flow of Geldart type A particles in a periodic domain were filtered to deduce residual correlations for the corresponding filtered TFM equations. Their approach has been verified for coarse grid simulations of fast fluidization in risers.[29,60] Note that gas-particle flows of Geldart type B particles are as well accessible by kinetic theory-based TFM, and, therefore, their model might be equally applicable to this type of flow. According to Eq. 3, their filtered drag coefficient reads[39]

$$\beta_{\mathrm{IS}}=\beta_{\mathrm{WY}}\left(1-f_{\mathrm{IS}}\left(\mathrm{Fr}_{\mathrm{filter}}\right)h_{\mathrm{IS}}\left(\epsilon_{\mathrm{s}}\right)g\left(\epsilon_{\mathrm{s}}\right)\right) \tag{19}$$

with the Froude number based on the filter length Δ_{filter}

$$\mathrm{Fr}_{\mathrm{filter}}^{-1}=\frac{g\Delta_{\mathrm{filter}}}{u_{\mathrm{t}}^2}$$

where the functions $f_{\mathrm{IS}}\left(\mathrm{Fr}_{\mathrm{filter}}\right)$, $h_{\mathrm{IS}}\left(\epsilon_s\right)$, and $g\left(\epsilon_{\mathrm{s}}\right)$ are fitted from the filtered highly resolved simulations. u_{t}^2 denotes the terminal settling velocity of a single particle. It is proposed that the characteristic length scale for filtering is given by u_{t}^2/g. Thus, the scaling, $f_{\mathrm{IS}}\left(\mathrm{Fr}_{\mathrm{filter}}\right)$, with the filter length reads

$$f_{\mathrm{IS}}\left(\mathrm{Fr}_{\mathrm{filter}}\right)=\frac{\mathrm{Fr}_{\mathrm{filter}}^{-1.6}}{\mathrm{Fr}_{\mathrm{filter}}^{-1.6}+0.4} \tag{20}$$

Grid sensitivity studies, in the case of a two-dimensional (2-D) riser, show that the grid spacing Δ should be less than half of the filter length,[60] that is

$$\Delta_{\mathrm{filter}} \ge 2\Delta \tag{21}$$

However, this condition for the filter length sounds arbitrary and no additional evidence is given for Eq. 21. Thus, to comply (21) we use $\Delta_{\mathrm{filter}}=3\Delta$ in this study. $h_{\mathrm{IS}}\left(\epsilon_s\right)$ and $g\left(\epsilon_{\mathrm{s}}\right)$ are solely functions of the filtered volume fraction ϵ_{s} and are given by

$$h_{\mathrm{IS}}(\epsilon_\mathrm{s}) = \begin{cases} 2.7\epsilon_\mathrm{s}^{0.234} & \epsilon_\mathrm{s} < 0.0012 \\ -0.019\epsilon_\mathrm{s}^{-0.455} + 0.963 & 0.0012 \le \epsilon_\mathrm{s} < 0.014 \\ 0.868\exp(-0.38\epsilon_\mathrm{s}) - 0.176\exp(-119.2\epsilon_\mathrm{s}) & 0.014 \le \epsilon_\mathrm{s} < 0.25 \\ -4.59 \cdot 10^{-5}\exp(19.75\epsilon_\mathrm{s}) + 0.852\exp(-0.268\epsilon_\mathrm{s}) & 0.25 \le \epsilon_\mathrm{s} < 0.455 \\ (\epsilon_\mathrm{s} - 0.59)\left(-150\epsilon_\mathrm{s}^3 + 2203\epsilon_\mathrm{s}^2 - 1054\epsilon_\mathrm{s} + 162\right) & 0.455 \le \epsilon_\mathrm{s} < 0.59 \\ 0 & \text{else} \end{cases} \tag{22}$$

and

$$g(\epsilon_\mathrm{s}) = \begin{cases} \epsilon_\mathrm{s}^{0.24}(1.48 + \exp(-18\epsilon_\mathrm{s}))) & \epsilon_\mathrm{s} < 0.18 \\ 1 & \epsilon_\mathrm{s} \ge 0.18 \end{cases} \tag{23}$$

Igci et al.[29] and Igci and Sundaresan[60] additionally introduced wall modifications of the filtered residual correlations for gas-particle flows in risers showing a significant reduction of the filtered drag near walls. Their correlation for the drag coefficient near walls, $\beta_{\mathrm{IS}}^{\mathrm{w}}$, reads

$$\beta_{\mathrm{IS}}^{\mathrm{w}} = \frac{1}{1 + 6e^{-a(\phi)x_\mathrm{d}}}\beta_{\mathrm{IS}}, \tag{24}$$

where $x_\mathrm{d} = gx/u_\mathrm{t}^2$ denotes the normalized dimensionless distance from the wall x. $a(\phi)$ is a function of the specularity coefficient ϕ appearing in the boundary conditions for collisional flows of Johnson and Jackson.[97] ϕ is a measure of the fraction of collisions transferring tangential momentum to the wall. It has to be noted that these boundary conditions do not distinguish between sliding and nonsliding particle wall collisions in the case of a constant specularity coefficient and thus, the tangential solids stresses at the wall are not limited by Coulomb friction[98,99] Additionally, several authors report that these boundary conditions may be unsuitable for general gas-particle flows.[16,23,24,33,100] The simulations of Igci and Sundaresan[60] revealed that

$$a(\phi) = 0.036\phi^2 + 0.162\phi + 0.295$$

However, the fluidized bed studied in the results section reveals that $x_\mathrm{d} < 0.43$ for all x. In the case of small values of x_d, the wall corrections appear nearly independent of ϕ and x yielding

$$\beta_{\mathrm{IS}}^{\mathrm{w}} \approx 0.175\beta_{\mathrm{IS}} \tag{25}$$

Thus, the additional drag modification does not seem to apply to our case and, therefore, we do not consider this correction.

Igci et al.[39] also reported a significant contribution to the filtered particle stresses arising from subfilter-scale Reynolds-stress-like velocity fluctuations, which appeared to be much larger than the particle stresses from kinetic theory. Thus, they concluded that the contribution of the filtered kinetic theory stresses could be neglected in a first approximation yielding a computationally efficient model for gas-particle flows in risers. However, while their simulations reveal a considerable filter length dependent contribution to the particle stresses in the collisional regime, the particle stresses do not show subfilter effects in the frictional regime. Noteworthy, our simulations reveal that the unresolved contribution of the particle stress influences, on the one hand, the predicted bed expansion and, on the other hand, the spatial particle distribution. The latter was also reported by Igci et al.[39] As a consequence, we consider the dominant contribution from subfilter-scale Reynolds-stress-like velocity fluctuations in this study.

Drag Model of Simonin's Group

The filtered drag correlation for dense fluidized beds of Geldart type A particles proposed by Simonin's group[28,59] has a very similar form to that of the Princeton group.[29,38,39,60] The filtered drag force reads

$$\boldsymbol{F}_\mathrm{P} = \beta_{\mathrm{WY}}\left(\mathbf{I} + f_\mathrm{P}(\Delta^*)h_\mathrm{P}(\widehat{\epsilon}_\mathrm{s})\mathbf{K}\right)\left(\boldsymbol{u}_\mathrm{g} - \boldsymbol{u}_\mathrm{s}\right) = \boldsymbol{\beta}_\mathrm{P}\left(\boldsymbol{u}_\mathrm{g} - \boldsymbol{u}_\mathrm{s}\right) \tag{26}$$

with $\tilde{\epsilon}_\mathrm{s} = \epsilon_\mathrm{s}/\epsilon_\mathrm{s}^{\max}$, the identity tensor $\mathbf{I}$ and the second rank tensors $\mathbf{K}$ and β_P. Note for one spatial dimension Eq. 26 reduces to

$$F_\mathrm{P} = \beta_\mathrm{P}\left(u_\mathrm{g} - u_\mathrm{s}\right) \tag{27}$$

where

$$\beta_\mathrm{P} = \beta_{\mathrm{WY}}\left(1 + f_\mathrm{P}(\Delta^*)h_\mathrm{P}(\widehat{\epsilon}_\mathrm{s})K\right)$$

The function $f_\mathrm{P}(\Delta^*)$ reveals the scaling with filter length

$$f_\mathrm{P}(\Delta^*) = \frac{\Delta^{*2}}{a^2 + \Delta^{*2}} \tag{28}$$

with $a \approx 0.0613$ and Δ^* reading as

$$\Delta^* = \frac{\Delta_{\mathrm{filter}}/\tau_\mathrm{p}^{\mathrm{St}}}{\sqrt{gD_\mathrm{h}}} \tag{29}$$

$\tau_\mathrm{p}^{\mathrm{St}}$ denotes the Stokes relaxation time of a single isolated particle defined as $\tau_\mathrm{p}^{\mathrm{St}} = \rho_\mathrm{s}d_\mathrm{s}^2/\left(18\mu_\mathrm{g}\right)$ and D_h the hydraulic diameter of fluidized bed. It is assumed that the filter length, Δ_{filter}, is related to the grid spacing by $\Delta_{\mathrm{filter}} = 2\Delta$, which is determined empirically by adjusting the bed height of a single coarse grid simulation. Analogous to Eq. 21, this choice seems also arbitrary and no additional indications are given about its general applicability. One important difference to the filtered drag correlation of the Princeton group is that the filter length is made dimensionless by using the bed diameter instead of the terminal settling particle velocity.[39] Additionally, Parmentier et al.[28] obtained from filtering fine grid simulations of a bubbling fluidized bed using Geldart type A particles

$$h_\mathrm{P}(\tilde{\epsilon}_\mathrm{s}) = -\sqrt{\tilde{\epsilon}_\mathrm{s}}(1 - \tilde{\epsilon}_\mathrm{s})^2\left(1 - 1.88\tilde{\epsilon}_\mathrm{s} + 5.16\tilde{\epsilon}_\mathrm{s}^2\right) \tag{30}$$

The values of the second rank tensor K_{ij} depend on the spatial direction and the simulation case, for example, the dimensions of the system and the inflow conditions. Due to geometrical properties it is assumed that $K_{ij} = 0$ for $i \ne j$ $(i, j \in \{x, y, z\})$. The remaining entries along the main diagonal K_{ii} are dynamically adjusted by adapting the methodology of Germano et al.[68] and Lilly.[69] First, a second filter, called test filter, is applied to the resolved quantities of the coarse grid simulation, that is,

$$\widehat{f}(\boldsymbol{x},t)=\frac{1}{7}\left(f(\boldsymbol{x},t)+\sum_{i}^{3}\left(f(\boldsymbol{x}+\Delta\boldsymbol{e}_i,t)+f(\boldsymbol{x}-\Delta\boldsymbol{e}_i,t)\right)\right) \tag{31}$$

with a characteristic length scale

$$\widehat{\Delta}_{\mathrm{filter}}=\Delta_{\mathrm{filter}}+\frac{24}{7}\Delta$$

and the unit vector $\boldsymbol{e}_i$ in i-th direction. Then, $\mathbf{K}$ can be evaluated from

$$\mathbf{K}=-\mathbf{L}\mathbf{M}^{-1} \tag{32}$$

with

$$\mathbf{L}=\mathbf{I}\left(\widehat{\epsilon_{\mathrm{s}}\boldsymbol{u}_{\mathrm{sg}}}-\widehat{\epsilon}_{\mathrm{s}}\widehat{\boldsymbol{u}}_{\mathrm{sg}}\right) \tag{33}$$

$$\mathbf{M}=\mathbf{I}\left(\left(\widehat{\epsilon_{\mathrm{s}}h(\tilde{\epsilon}_{\mathrm{s}})\boldsymbol{u}_{\mathrm{sg}}}\right)f_{\mathrm{P}}(\Delta^{*})-\widehat{\epsilon}_{\mathrm{s}}h\left(\widehat{\tilde{\epsilon}}_{\mathrm{s}}\right)\widehat{\boldsymbol{u}}_{\mathrm{sg}}f_{\mathrm{P}}\left(\widehat{\Delta}^{*}\right)\right) \tag{34}$$

where $\boldsymbol{u}_{\mathrm{sg}}=\boldsymbol{u}_{\mathrm{s}}-\boldsymbol{u}_{\mathrm{g}}$, $\widehat{\boldsymbol{u}}_{\mathrm{sg}}=\widehat{\boldsymbol{u}}_{\mathrm{s}}-\widehat{\boldsymbol{u}}_{\mathrm{g}}$, $\widehat{\boldsymbol{u}}_{\mathrm{s}}=\widehat{\epsilon_{\mathrm{s}}\boldsymbol{u}_{\mathrm{s}}}/\widehat{\epsilon}_{\mathrm{s}}$, and $\widehat{\boldsymbol{u}}_{\mathrm{g}}=\widehat{\epsilon_{\mathrm{g}}\boldsymbol{u}_{\mathrm{g}}}/\widehat{\epsilon}_{\mathrm{g}}$. $\widehat{\Delta}^{*}$ is the dimensionless form of $\widehat{\Delta}_{\mathrm{filter}}$ according to Eq. 29.

Finally, in the case of the fluidized bed studied in Parmentier et al.,[28] K_{zz} appears nearly independent of the vertical coordinate and is approximately 4 for $\Delta=64d_{\mathrm{s}}$. In this study, we investigate a dynamically adjusted, that is $\mathbf{K}$ evaluated from Eq. 32 (denoted by $\boldsymbol{\beta}_{\mathrm{P}}$), and an unadjusted case, that is $\mathbf{K}=\mathbf{I}$ (denoted by β_{P}). Note, β_{P} and β_{IS} (without wall corrections) only differ in form of the scaling with the filter length.

CD-Lab Model

Schneiderbauer et al.[42] obtained a grid-dependent expression for H_{d}, which followed the idea of the formation of clusters inside a fluidized bed described by Eqs. 4–13 (compare also with Figure 1). For Geldart B and D particles it is reasonable to assume that $\mathcal{O}\left(\epsilon_{\mathrm{s}}^{\mathrm{d}}\right)\ll\mathcal{O}\left(\epsilon_{\mathrm{s}}^{\mathrm{c}}\right)$,[27] which implies $\epsilon_{\mathrm{g}}^{\mathrm{d}}\approx 1$. In this case, $\epsilon_{\mathrm{s}}^{\mathrm{d}}\boldsymbol{u}_{\mathrm{s}}^{\mathrm{d}}f^{\mathrm{d}}\ll\epsilon_{\mathrm{s}}^{\mathrm{c}}\boldsymbol{u}_{\mathrm{s}}^{\mathrm{c}}f^{\mathrm{c}}$ and this, in turn, implies $\epsilon_{\mathrm{s}}^{\mathrm{c}}\boldsymbol{u}_{\mathrm{s}}^{\mathrm{c}}f^{\mathrm{c}}\approx\epsilon_{\mathrm{s}}\boldsymbol{u}_{\mathrm{s}}$. By using $\epsilon_{\mathrm{s}}^{\mathrm{c}}f^{\mathrm{c}}\approx\epsilon_{\mathrm{s}}$ Eqs. 11–13 reduce to

$$\epsilon_{\mathrm{g}}\boldsymbol{u}_{\mathrm{g}}=\boldsymbol{u}_{\mathrm{g}}^{\mathrm{d}}f^{\mathrm{d}}+\epsilon_{\mathrm{g}}^{\mathrm{c}}\boldsymbol{u}_{\mathrm{g}}^{\mathrm{c}}f^{\mathrm{c}} \tag{35}$$

$$\boldsymbol{u}_{\mathrm{s}}=\boldsymbol{u}_{\mathrm{s}}^{\mathrm{c}} \tag{36}$$

$$\epsilon_{\mathrm{g}}=f^{\mathrm{d}}+\epsilon_{\mathrm{g}}^{\mathrm{c}}f^{\mathrm{c}} \tag{37}$$

In this limit, $\boldsymbol{F}_{\mathrm{d}}^{\mathrm{d}}$ is negligible compared to $\boldsymbol{F}_{\mathrm{d}}^{\mathrm{cl}}$ and $\boldsymbol{F}_{\mathrm{d}}^{\mathrm{c}}$, and hence, Eq. 4 yields

$$\boldsymbol{F}_{\mathrm{d}}^{\mathrm{cl}}\approx f^{\mathrm{d}}\boldsymbol{F}_{\mathrm{d}}^{\mathrm{c}} \tag{38}$$

If the voidage within clusters, $\epsilon_{\mathrm{g}}^{\mathrm{c}}$, is known, the fraction of clusters can be computed from Eq. 37 as follows

$$f^{\mathrm{c}}=\frac{1-\epsilon_{\mathrm{g}}}{1-\epsilon_{\mathrm{g}}^{\mathrm{c}}}=\frac{\epsilon_{\mathrm{s}}}{\epsilon_{\mathrm{s}}^{\mathrm{c}}} \tag{39}$$

Wang et al.[54] proposed that

$$\epsilon_{\mathrm{g}}^{\mathrm{c}}=\epsilon_{\mathrm{g}}-n\sigma_{\epsilon} \tag{40}$$

with $n=2$. σ_{ϵ} denotes the standard deviation of the fluctuations of the solids volume fraction. Based on a doubly stochastic Poisson process, that is, the number of particles in a cluster follows a negative exponential distribution[81] and these randomly distributed particles inside a cluster follow a Poisson distribution, Wang et al.[54] calculated σ_{ϵ} as

$$\sigma_{\epsilon}=\epsilon_{\mathrm{s}}\sqrt{S(\epsilon_{\mathrm{s}})} \tag{41}$$

where $S(\epsilon_{\mathrm{s}})$ is the static structure factor in the small wave vector limit written as

$$S(\epsilon_{\mathrm{s}})=\frac{(1-\epsilon_{\mathrm{s}})^4}{1+4\epsilon_{\mathrm{s}}+4\epsilon_{\mathrm{s}}^2-4\epsilon_{\mathrm{s}}^3+\epsilon_{\mathrm{s}}^4} \tag{42}$$

However, Eq. 40 does not approach $1-\epsilon_{\mathrm{s}}^{\max}$ as ϵ_{s} tends to $\epsilon_{\mathrm{s}}^{\max}$ although no heterogenous structures exist at maximum packing. The requirement $\sigma_{\epsilon}\left(\epsilon_{\mathrm{s}}^{\max}\right)=0$ is also supported by experimental data.[101] We, therefore, propose to replace the constant n in Eq. 40 by

$$\tilde{n}=\frac{1}{2}n\tanh\left(\frac{\epsilon_{\mathrm{s}}-\epsilon_{\mathrm{s}}^{\mathrm{blend}}}{\sigma_{\epsilon}^{\mathrm{blend}}}\right) \tag{43}$$

which is consistent with the data of Manyele et al.[102] yielding $\epsilon_{\mathrm{s}}^{\mathrm{blend}}\approx 0.3$ and $\sigma_{\epsilon}^{\mathrm{blend}}\approx 0.15$.

Furthermore, a closure for the cluster diameter, d_{cl}, is required. For Geldart type A particles and fast fluidization the probability density function of the normalized cluster diameter, $\xi=d_{\mathrm{cl}}/d_{\mathrm{s}}$ was determined experimentally, for example, by Zou et al.[81] reading as

$$p(\xi)=A\exp\left(-\frac{(\xi-1)^b}{\delta}\right) \tag{44}$$

with $\delta=\epsilon_{\mathrm{s}}^{n_1}\left(\epsilon_{\mathrm{s}}^{\mathrm{mf}}-\epsilon_{\mathrm{s}}\right)^{-n_2}\epsilon_{\mathrm{g}}^{-n_3}$ and A is determined by $\int_1^{\infty}p(\xi)\mathrm{d}\xi=1$. $\epsilon_{\mathrm{s}}^{\mathrm{mf}}$ denotes the solids volume fraction at minimum fluidization conditions. By correlating with their experimental data, the following parameters were obtained[81]: $b=0.72$, $n_1=0.25$, $n_2=2.41$, and $n_3=1.5$. Note that the present study aims on the application of the CD-Lab drag modification to a bubbling fluidized bed of Geldart B particles. However, to the authors' knowledge, there is no literature specifying the probability density function of the particle cluster diameter of Geldart type B particles, and thus, in a first step, we use Eq. 44.

The average cluster diameter as a function of the solids volume fraction yields

$$\langle\xi\rangle_{\infty}=\int_1^{\infty}\xi p(\xi)\mathrm{d}\xi\approx 1.8543\delta^{1.3889}+1 \tag{45}$$

This result corresponds well with other data from literature.[103,104] It is observed that the mean cluster diameter is a monotonically increasing function with the mean solids volume fraction and diverges at $\epsilon_{\mathrm{s}}^{\mathrm{mf}}$. Physically, this behavior is reasonable as no fluidization occurs above $\epsilon_{\mathrm{s}}^{\mathrm{mf}}$, and the homogenous distribution of the particles is recovered. However, clusters greater than the grid spacing Δ are resolved by the grid and, therefore, require no additional modeling. In this case, according to the assumption of uniformly distributed particles inside a cluster, homogenous conditions in a numerical cell establish and β_{WY} (Eq. 58) would be applicable directly. Therefore, we propose to use the expectation value of the unresolved clusters for d_{cl}, that is

$$d_{\mathrm{cl}}=d_{\mathrm{s}}\langle\xi\rangle_{\Delta}\qquad\text{with}\qquad\langle\xi\rangle_{\Delta}=\int_1^{\Delta/d_{\mathrm{s}}}\xi p(\xi)\mathrm{d}\xi \tag{46}$$

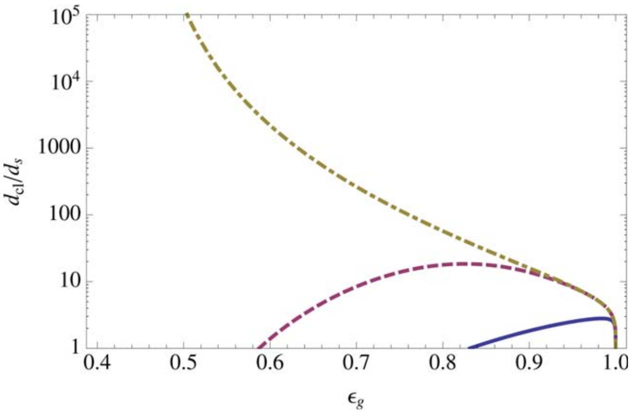

Figure 2. The dimensionless average cluster diameter $\langle\xi\rangle_\Delta = d_{\mathrm{cl}}/d_{\mathrm{s}}$ as a function of the mean voidage ϵ_{g} ($\epsilon_{\mathrm{s}}^{\mathrm{mf}}=0.55$) for different grid spacings: —— $8d_{\mathrm{s}}$; – – $64d_{\mathrm{s}}$; – · – ∞ (as used in EMMS[26,54,57]).

[Color figure can be viewed in the online issue, which is available at wileyonlinelibrary.com.]

The antiderivative in Eq. 46 can be evaluated by the substitution $\zeta=\xi-1$, which yields

$$d_{\mathrm{cl}}=d_{\mathrm{s}}\int_0^{\Delta/d_{\mathrm{s}}-1}(\zeta+1)p(\zeta)\mathrm{d}\zeta \tag{47}$$

Integration gives

$$d_{\mathrm{cl}}=d_{\mathrm{s}}\frac{\Gamma\left(\bar{b}\right)-\Gamma\left(\bar{b},\bar{\Delta}\right)+\delta^{1/b}\left(\Gamma\left(2\bar{b}\right)-\Gamma\left(2\bar{b},\bar{\Delta}\right)\right)}{b\Gamma\left(1+\bar{b}\right)} \tag{48}$$

with

$$\bar{b}=b^{-1} \qquad \text{and} \qquad \bar{\Delta}=\left(\frac{\Delta}{d_{\mathrm{s}}}-1\right)^b\delta^{-1}$$

$\Gamma(a,z)$ denotes the incomplete Gamma function given by

$$\Gamma(a,z)=\int_z^\infty t^{a-1}e^{-t}\mathrm{d}t$$

Note that $\Gamma(a)=\Gamma(a,0)$. As Δ approaches ∞, d_{cl} tends to result of Eq. 45, that is

$$\lim_{\Delta\to\infty} d_{\mathrm{cl}}=d_{\mathrm{s}}\langle\xi\rangle_\infty \tag{49}$$

In Figure 2, the expectation value of the dimensionless cluster diameter $\langle\xi\rangle_\Delta=d_{\mathrm{cl}}/d_{\mathrm{s}}$ is plotted as a function of the mean voidage ϵ_{g}. The figure shows that for grid spacings of $\mathcal{O}(\Delta)<\mathcal{O}(8d_{\mathrm{s}})$ the unresolved clusters only have a minor effect on regions of high voidage, that is, $\epsilon_{\mathrm{g}}>0.85$. Thus, in the case of fluidized beds, where regions of low voidage are predominant, a homogenous drag law can be applied for grid spacings $\Delta\lesssim 10d_{\mathrm{s}}$.[47] In contrast, for grid spacings of $\mathcal{O}(\Delta)>\mathcal{O}(64d_{\mathrm{s}})$ clusters containing a huge number of particles are present for nearly the whole range of ϵ_{g} indicating pronounced heterogenous subgrid structures, which require additional modeling in the sense of Eqs. 35–38.

To sum up, we have closed the system of Eqs. 35–38 by assumptions about the void fraction inside a cluster (Eq. 40) and the mean unresolved cluster diameter (Eq. 48). However, the fluid velocity in the dilute region, $\boldsymbol{u}_{\mathrm{g}}^{\mathrm{c}}$, and the fluid velocity inside a cluster, $\boldsymbol{u}_{\mathrm{g}}^{\mathrm{c}}$ remain unknown. These can be obtained from the following nonlinear system of equations

$$\boldsymbol{D}\left(\boldsymbol{u}_{\mathrm{g}}^{\mathrm{d}},\boldsymbol{u}_{\mathrm{g}}^{\mathrm{c}}\right)=\begin{pmatrix}\epsilon_{\mathrm{g}}\boldsymbol{u}_{\mathrm{g}}-\boldsymbol{u}_{\mathrm{g}}^{\mathrm{d}}f^{\mathrm{d}}-\epsilon_{\mathrm{g}}^{\mathrm{c}}\boldsymbol{u}_{\mathrm{g}}^{\mathrm{c}}f^{\mathrm{c}}\\ \boldsymbol{F}_{\mathrm{d}}^{\mathrm{cl}}-f^{\mathrm{d}}\boldsymbol{F}_{\mathrm{d}}^{\mathrm{c}}\end{pmatrix}=0 \tag{50}$$

with $\boldsymbol{u}_{\mathrm{s}}=\boldsymbol{u}_{\mathrm{s}}^{\mathrm{c}}$ and $f^{\mathrm{d}}+f^{\mathrm{c}}=1$. Equation 50 can be solved iteratively by applying Newton's method or Broydon's method.

Finally, the effective drag coefficient including subgrid structures may read as

$$\beta_{\mathrm{CL}}=\frac{1}{||\boldsymbol{u}_{\mathrm{g}}-\boldsymbol{u}_{\mathrm{s}}||}||\boldsymbol{F}_{\mathrm{d}}^{\mathrm{cl}}+f^{\mathrm{c}}\boldsymbol{F}_{\mathrm{d}}^{\mathrm{c}}|| \tag{51}$$

where $\boldsymbol{F}_{\mathrm{d}}^{\mathrm{cl}}$ and $\boldsymbol{F}_{\mathrm{d}}^{\mathrm{d}}$ can be computed from the solution of Eq. 50.

Comparison of Drag Modifications

In Figure 3, the heterogeneity indices $H_{\mathrm{d}}^i=\beta_i/\beta_{\mathrm{WY}}$ ($i\in\{\mathrm{E},\mathrm{K},\mathrm{IS},\mathrm{P},\mathrm{CL}\}$) for the discussed drag modifications are plotted as a function of the mean voidage for different slip velocities and grid spacings (filter lengths).

Figure 3e shows that $H_{\mathrm{d}}^{\mathrm{CL}}\ll 1$, that is, compared to the homogeneous correlation β_{WY} the effective drag β_{CL} is significantly reduced, at voidages ϵ_{g} with large unresolved clusters. Next, $H_{\mathrm{d}}^{\mathrm{CL}}$ slightly increases for increasing slip velocity $u_{\mathrm{s}}^{\mathrm{sl}}$, which is in accordance with the predictions of the EMMS model, β_{E} (Figure 3a). In contrast, we observe from Figures 3b and f that β_{K} is considerably reduced with increasing slip velocity, whereas β_{IS} and β_{P} do not show any dependence on the slip velocity (Figures 3c and d).[28,29,38,39,60] For very low slip velocities, that is, $\epsilon_{\mathrm{g}}u_{\mathrm{s}}^{\mathrm{sl}}\approx\epsilon_{\mathrm{g}}^{\mathrm{mf}}u_{\mathrm{g}}$, β_{K} even reveals $H_{\mathrm{d}}>1$ for a wide range of gas volume fractions. This is not observed for the other drag modifications.

Given that the expectation value of the diameter of the unresolved clusters increases with increasing grid spacing Δ, $H_{\mathrm{d}}^{\mathrm{CL}}$ decreases with increasing grid spacing (Figure 3e). This is in contrast to the EMMS model, which does not distinguish between resolved and unresolved clusters. This, in turn, implies that EMMS predicts a significantly lower heterogeneity index than the CD-Lab model in the dense regime (low voidage), where the clusters may be resolved by the grid (Figure 3a). Remarkably, $H_{\mathrm{d}}^{\mathrm{E}}$ even decreases again as the solids volume fraction approaches the maximum packing, which is not supported by fine grid simulations.[28,39,60] For solids volume fractions above the minimum fluidization point, the prevailing frictional stresses may also homogenize the granular assembly and, therefore, H_{d} should reach unity for $\epsilon_{\mathrm{s}}>\epsilon_{\mathrm{s}}^{\mathrm{mf}}$ as predicted by $H_{\mathrm{d}}^{\mathrm{CL}}$, $H_{\mathrm{d}}^{\mathrm{IS}}$, and $H_{\mathrm{d}}^{\mathrm{P}}$. As the EMMS model $H_{\mathrm{d}}^{\mathrm{K}}$ does not distinguish between resolved bubbles and unresolved bubbles. Thus, $H_{\mathrm{d}}^{\mathrm{K}}$ decreases for decreasing voidage as long as $\epsilon_{\mathrm{g}}>\epsilon_{\mathrm{g}}^{\mathrm{mf}}$ but is set to unity for $\epsilon_{\mathrm{g}}<\epsilon_{\mathrm{g}}^{\mathrm{mf}}$ according to the above arguments (Figure 3b). Thus, $H_{\mathrm{d}}^{\mathrm{E}}$ and $H_{\mathrm{d}}^{\mathrm{K}}$ prescribe a mesh size independent modification of the homogeneous drag coefficient, and may be regarded as the large filter length (grid spacing) limit. As a consequence, both do not approach unity for sufficiently fine grids, and this, in turn, implies that these do not recover the homogenous drag correlation in this limit.

Figures 3c and d reveal that $H_{\mathrm{d}}^{\mathrm{IS}}$ and $H_{\mathrm{d}}^{\mathrm{P}}$ decrease with increasing grid spacings, which requires higher-filter lengths ($\Delta_{\mathrm{filter}}\gtrsim 2\Delta$). Both show an asymptotic behavior for large

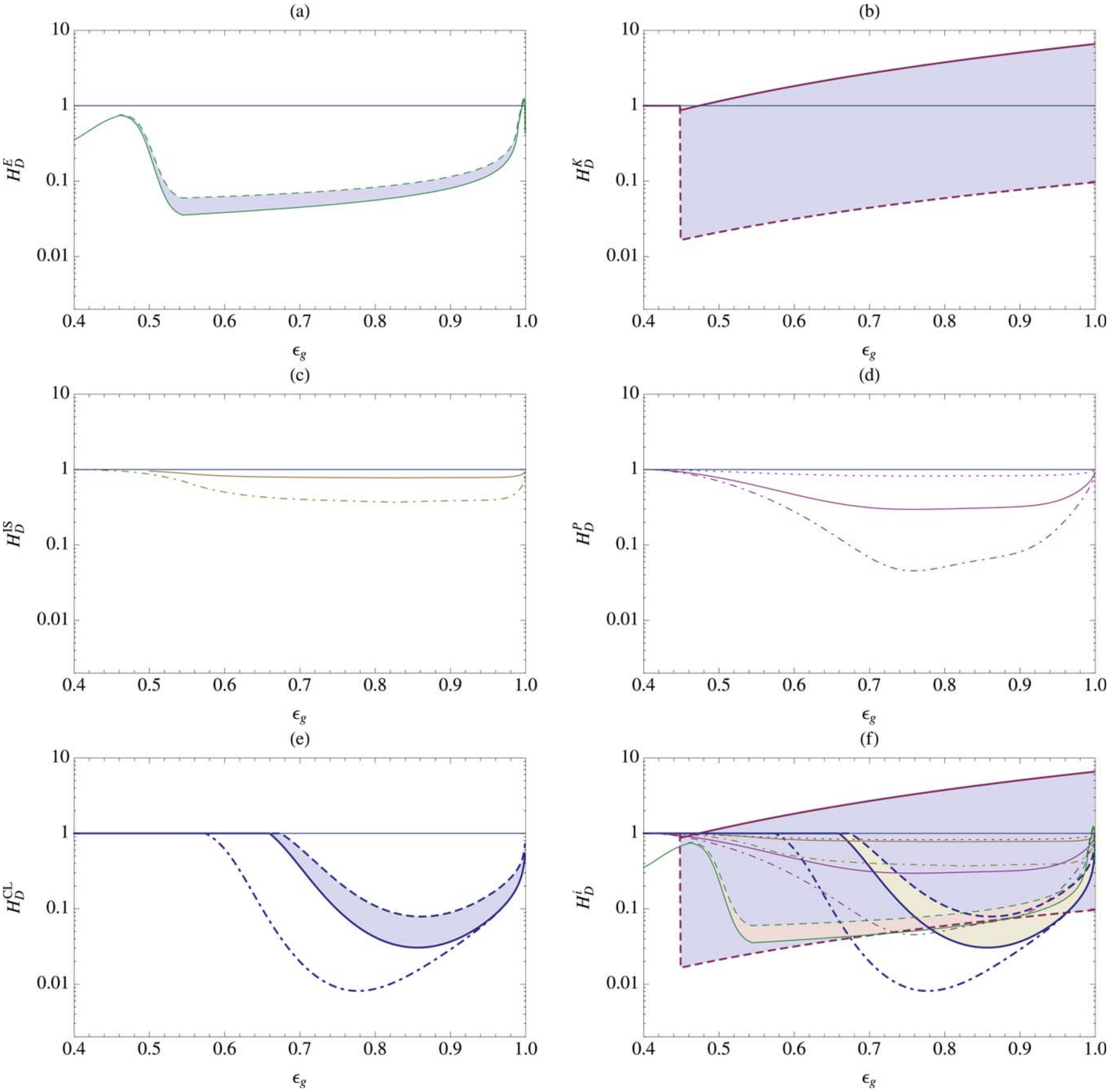

Figure 3. Heterogeneity index $H_d^i=\beta_i/\beta_{WY}$ ($i\in\{E, K, IS, P, CL\}$) for $\rho_s=2500$ kg s^{-1} and $d_s=150$ μm as a function of the mean voidage ϵ_g for different grid spacings and slip velocities $u_s^{sl}=||u_g-u_s||$ in the case of the bubbling fluidized bed presented in the results section ($\epsilon_s^{mf}=0.55$): — $\Delta=64d_s$ with $u_s^{sl}=0.2$ m s^{-1}; – – $\Delta=64d_s$ with $u_s^{sl}=5$ m s^{-1}; – · – $\Delta=256d_s$ ($\equiv D_h$) with $u_s^{sl}=0.2$ m s^{-1}. (a) H_d^E (Table 1), (b) H_d^K (Eq. 16), (c) H_d^{IS} (Eq. 19), (d) H_d^P (Eq. 26): — and – · –$K=4I$, $\cdots$ $K=I$ with $\Delta=64d_s$, (e) H_d^{CL} (Eq. 51), and (f) comparison of drag modifications; the shaded areas emphasize drag modifications depending on the slip velocity.

[Color figure can be viewed in the online issue, which is available at wileyonlinelibrary.com.]

filter lengths (e.g., Δ in the order of the bed diameter). In this case, H_d^{CL} shows a different asymptotical behavior (compare with Eq. 64), yielding $H_d^{CL}(\Delta=D_h)\ll H_d^{IS}(\Delta=D_h)$ and $H_d^{CL}(\Delta=D_h)\ll H_d^{P}(\Delta=D_h)$ (Figure 3f). This is attributed to the assumption of homogenous conditions within clusters, which is, however, crucial in the case of large clusters, where again clusters may form inside the larger clusters.

Although, H_d^{IS} and H_d^{P} use different scalings with filter length, that is the terminal settling velocity for H_d^{IS} (Eq. 20) and the hydraulic diameter of the bed for H_d^{P} (Eq. 28), both reveal similar heterogeneity indices for 150 μm particles in the case of the unadjusted β_P (Figures 3c, d, and f). Furthermore, both heterogeneity indices tend to unity as the particle diameter increases, when the ratio Δ/d_s is kept constant. In contrast, H_d^{CL} does not reveal such a trend as it depends on Δ/d_s. However, the large filter limits are not affected by the particle diameter. Significant differences between H_d^{IS} and H_d^{P} establish as the extensions of the fluidized bed become large. In this case, f_P tends to zero implying $\lim_{D_h\to\infty}H_d^{P}=1$

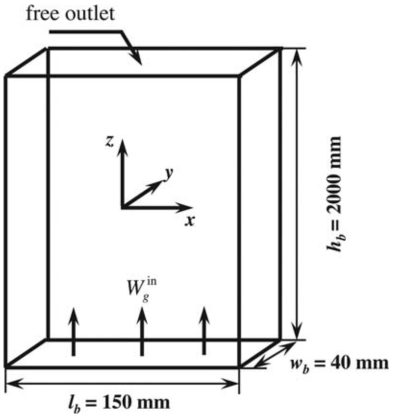

Figure 4. Sketch of the bubbling fluidized bed geometry.

At the bottom gas is distributed homogeneously to the bed with a superficial gas velocity W_g^{in}.

and, therefore, no drag modification is applied whereas H_d^{IS} remains unchanged.

Finally, it has to be noted that β_K does not reveal continuous behavior at ϵ_g^{mf} as claimed by Wang et al.[27] (Figure 3b). In contrast, all the others are continuous for reasonable ϵ_g (Figure 3f). It is noteworthy that none of the drag modifications depends on particle properties, for example, the particle–particle restitution coefficient e_s, which is consistent with the data of Igci and Sundaresan.[60]

Bubbling Fluidized Bed

To study the subgrid drag correlations in the bubbling/slugging regime, we investigated a gas–solid fluidized bed of Geldart B glass particles. Two simple cases with different superficial vertical gas velocities $W_g^{\text{in}} = 0.21$ m s^{-1} and $W_g^{\text{in}} = 0.63$ m s^{-1} at the inflow are studied by using the TFM model for gas-particle flows of Schneiderbauer et al.,[23] which is summarized in the Appendix. At the side walls, we apply a no-slip boundary condition for the gas phase and a partial slip boundary conditions for the solid phase (Table 4 and Figure 4). The physical parameters are given in Table 2. Thus, the ratio of the superficial gas velocity and the terminal settling velocity of an isolated particle is between 0.22 and 0.7, which is less than that for the case studied in Parmentier et al.[28]

The dimensions of the fluidized bed are given in Figure 4. Note these correspond to our in-house experiment, which will be used for future validation studies.

Following our previous studies,[23,24,42] we apply the computational fluid dynamics solver FLUENT (version 14) to solve the model equations (Table 3), whereby Eqs. 9, 16, 19, 27, 51, and 60–70 are not covered by its standard functional range. These are, therefore, implemented by user defined functions. For the discretization of the convective terms appearing in the transport Eqs. 54, 55, 56 and 57, a second-order upwind scheme is used. The derivatives appearing in the diffusion terms in Eqs. 55–57 are computed by a least squares method, and the pressure–velocity coupling is achieved by the SIMPLE algorithm, whereas the face pressures are computed as the average of the pressure values in the adjacent cells (linear interpolation). The time step size is set adaptively to comply

$$\max_{q,\Omega} \text{CFL}_{q,\Delta} < 1$$

at every time step, where $\text{CFL}_{q,\Delta}$ denotes the Courant number of phase q based on the grid spacing Δ and Ω is the simulation domain.

Low superficial gas velocity: $W_g^{in} = 0.21 ms^{-1}$

We obtained a time-dependent solution using a grid spacing $\Delta_f = 8d_s$, which is assumed to be sufficiently fine to resolve all heterogeneous structures,[47] referred to as reference solution. Thus, we used the homogenous drag correlation in Eq. 58, that is, $\beta_i \equiv \beta_{WY}$ for $\Delta \lesssim 10d_s$ in the case of fluidized beds. Note β_E and β_K do not reveal the homogenous drag correlation in the fine grid limit as discussed in the last section. To study the effect of subgrid structures on the behavior of the fluidized bed, for example, the bed expansion, we repeated this simulation using a grid spacing of $\Delta_c = 64d_s$ (coarse grid) with β_i with $i \in \{\text{E}, \text{K}, \text{IS}, \text{P}, \text{CL}, \text{WY}\}$.

Particle Volume Fraction. In Figure 5a, a comparison of the time-averaged axial profile of the solids volume fraction ϵ_s for $W_g^{\text{in}} = 0.21$ m s^{-1} is shown. First, it is observed that neglecting subgrid heterogeneity, that is, $\beta \equiv \beta_{WY}$, leads to a significant overprediction of the bed expansion using the coarse grid. In fact, the bed expansion is overestimated considerably (by ca. 80%) compared to the fine grid reference simulation, which is generally agreed.[26–32] This, in turn, implies that using the homogenous drag correlation on coarse grids underestimates the time averaged volume fractions within the bed (Figure 6). Furthermore, Figure 5b shows that the coarse grid simulation generally underestimates the standard deviation of the time averaged solids volume fraction. This gives evidence of less pronounced bubbling of the fluidized bed using the coarse grid. In other words, the particles are predicted to be less heterogeneously distributed and no distinct bubbles form, which is also confirmed by comparing snapshots of the spatial distribution of the solids volume fraction (Figures 7a, b, and i).

Table 2. Physical Parameters (for Reference See[23,27,61,64,67,105,106])

Property		Value	Unit
particle diameter	d_s	150	μm
particle density	ρ_s	2500	kg m^{-3}
gas density	ρ_g	1.224	kg m^{-3}
solids volume fraction at minimum fluidization conditions	ϵ_s^{mf}	≈ 0.55	–
solids volume fraction at maximum packing	ϵ_s^{max}	0.6	–
initial bed height	h_0	0.5	m
bed height at minimum fluidization conditions	h^{mf}	h_0	m
initial solids volume fraction	$\epsilon_{s,0}$	0.55	–
gas velocity at minimum fluidization conditions	u_g^{mf}	≈ 0.18	m s^{-1}
superficial gas velocity at minimum fluidization conditions	U_g^{mf}	≈ 0.08	m s^{-1}
terminal settling velocity of an isolated particle	u_t	0.96	m s^{-1}
coefficient of wall friction	μ_w	0.5	–
coefficient of restitution for particle–particle collisions	e_s	0.9	–
coefficient of restitution for particle–wall collisions	e_w	0.9	–
tangential restitution coefficient	β_0	0.4	–

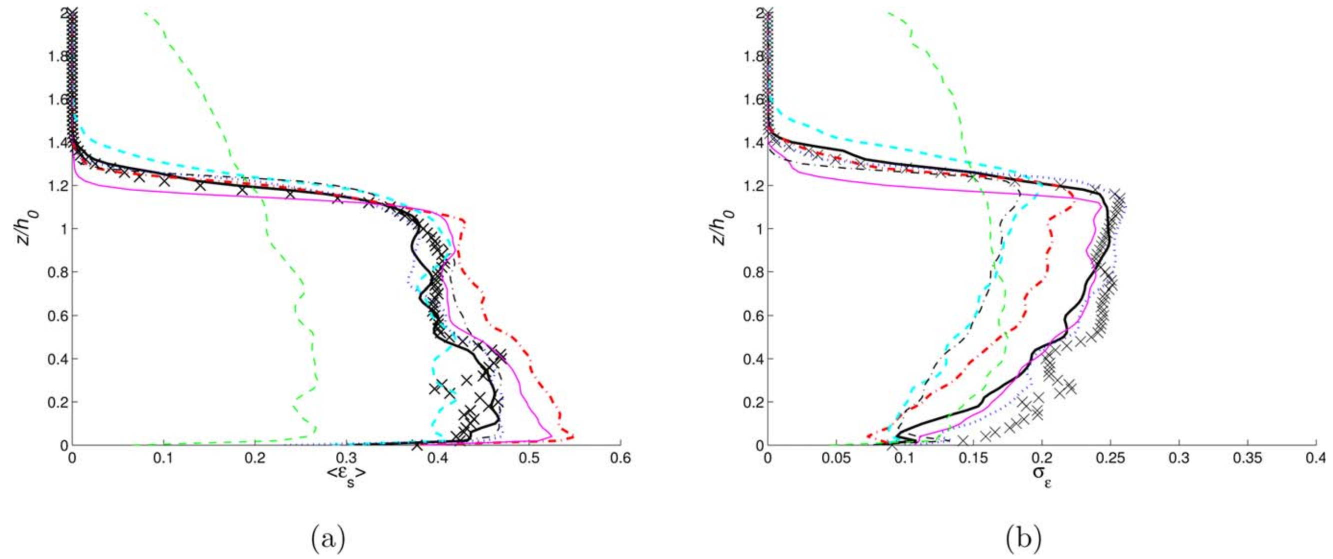

(a) (b)

Figure 5. Axial profiles of the time averaged solids volume fraction, <ϵ_s>, and its standard deviation, σ_ϵ, for $W_g^{in}=0.21$ m s^{-1} and $\Delta_c=64d_s$ (the averaging time is 10 s): —— β_{CL} (Eq. 51); —.— β_P (Eq. 26); — — — β_P (K = 1) (Eq. 27); . . . . β_K (Eq. 16); —— β_E EMMS (Eq. 9); – · –β_{IS} (Eq. 19); – – –β_{WY} (Eq. 58); × β_{WY} with $\Delta_f=8d_s$ (Eq. 58). Note the results of the fine grid simulation are displayed on the coarse grid by applying a box filter with filter length Δ_c.

[Color figure can be viewed in the online issue, which is available at wileyonlinelibrary.com.]

Second, we investigated the behavior of the fluidized bed when applying the different subgrid drag closures β_i ($i \in \{\mathrm{E, K, IS, P, CL}\}$) on the coarse grid ($\Delta_c=64d_s$). Remarkably, although these reveal significant different dependencies on u_s^{sl} and ϵ_g Figure 5a clearly demonstrates that the predicted bed expansions are in fairly good agreement with the fine grid data (compare also with Figure 7). Our results show that applying the dynamic adjustment procedure in the case of $\boldsymbol{\beta}_\mathrm{P}$ slightly improves the agreement with the reference solution with respect to the bed expansion. It is noteworthy that accounting for the subgrid stress contribution in the case of β_{IS} appears to considerably increase the correlation of the predicted spatial particle distribution with the fine grid simulation when compared to the equivalent drag correction β_P (compare with Figure 3). Thus, the different characteristic length scales used for filtering u_t^2/g and $\tau_p^{St}\sqrt{gD_h}$ seem to be appropriate in this case, although, it is observed that H_d^{IS} and $H_d^P(K=1)$ rapidly approach unity as the particle diameter increases even for filter lengths of several hundreds of particle diameters. In particular, the studies of[28,38,39,60] are based on particles with $d_s < 100$ μm (Geldart type A). Finally, β_E yields a slightly lower bed expansion than β_{CL}, which can be attributed to the low values of H_d^E at low voidages, that is, in the frictional regime, where the others recover the homogenous drag and especially H_d^K is set to unity. Furthermore, β_E may

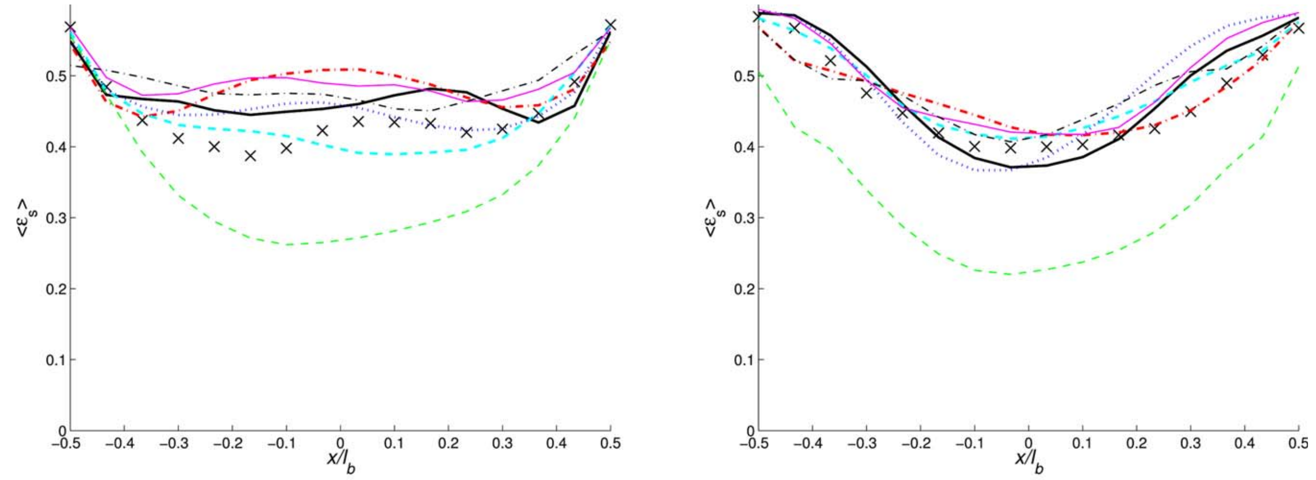

(a) (b)

Figure 6. Horizontal profiles in the middle plane of the time averaged solids volume fraction, ϵ_s, for $W_g^{in}=0.21$ m s^{-1} and $\Delta_c=64d_s$ (the averaging time is 10 s).

The lines and symbols have the same meaning as in Figure 5. Note the results of the fine grid simulation are displayed on the coarse grid by applying a box filter with filter length Δ_c. l_b (=150 mm) denotes the length of the bed. [Color figure can be viewed in the online issue, which is available at wileyonlinelibrary.com.]

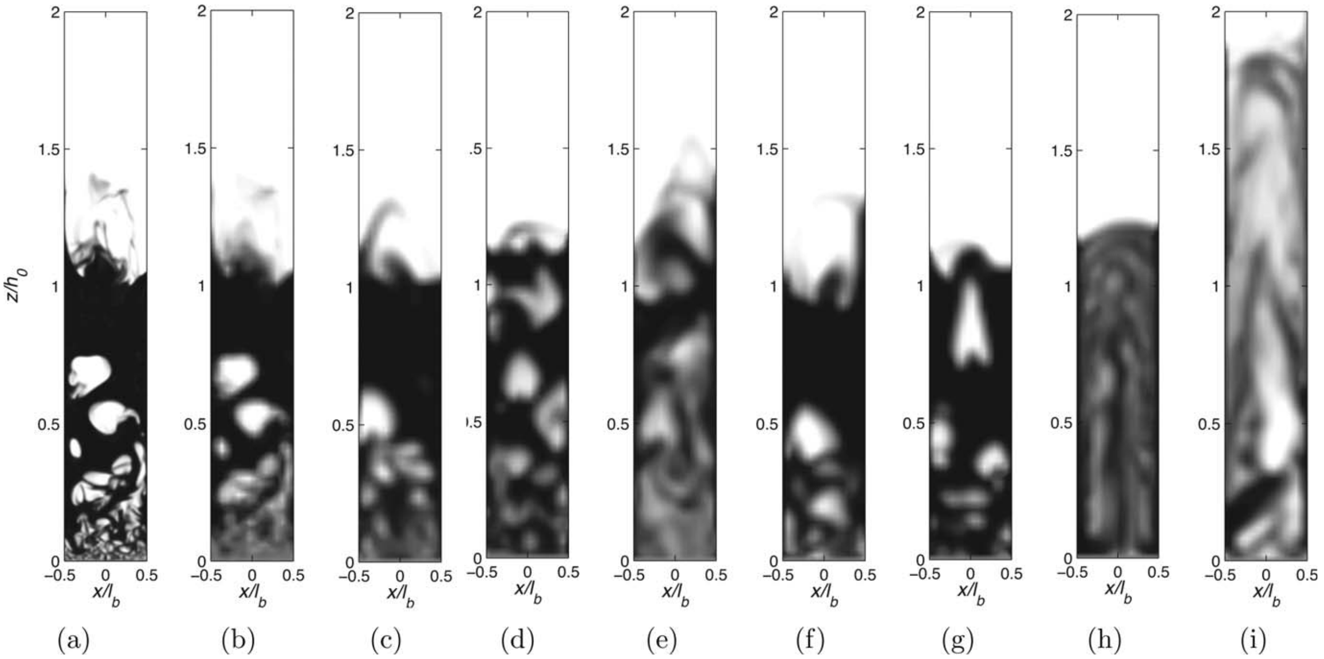

Figure 7. Snapshots of the solids volume fraction, ϵ_s, at t = 10 s for W_g^{in} =0.21 m s^{-1} (white: ϵ_s=0; black: $\epsilon_s=\epsilon_s^{max}$). (a) fine grid, (b) fine grid with applied box filter with $l_\Delta=\Delta$, (c) coarse grid using β_{CL} (Eq. 51), (d) coarse grid using β_P (Eq. 26), (e) coarse grid using β_P (K = 1) (Eq. 27), (f) coarse grid using β_K (Eq. 16), (g) coarse grid using β_E (Eq. 9), (h) coarse grid using β_{IS} (Eq. 19), and (i) coarse grid using β_{WY} (Eq. 58). l_b (=150 mm) denotes the length of the bed.

The figure shows distinct bubbles for $\boldsymbol{\beta}_P$, β_{CL}, β_K, β_E and blurred bubbles for β_P (K =1), β_{IS}, and β_{WY}.

represent the large grid limit of H_d as mentioned in the previous section, which, in turn, implies an overestimation of the drag reduction in the case of intermediate grid sizes (Δ_c=64d_s).

Figure 5a also shows that all subgrid drag modifications predict the axial time-averaged profile of the solids volume fraction appropriately, which is characterized by higher-particle concentrations in the gas-inflow area, that is, $\langle\epsilon_s\rangle \approx 0.45$ for $z/h_0 < 0.6$ and lower particle concentrations at lower hydrostatic pressure, that is, $\langle\epsilon_s\rangle \approx 0.4$ for $z/h_0 > 0.6$.

The horizontal profiles of the time averaged volume fraction (Figure 6) confirm that the subgrid modifications of the drag force reveal particle accumulation at the side walls and bubble accretion in the center of the bed as observed from the fine grid simulation. However, on the coarse grid this tendency is more pronounced than on the fine grid supporting the demand of wall corrections.[60]

From Figure 5b, we deduce two classes of subgrid drag models. Models preserving the bubbling regime and models, which do not preserve bubbling. Even though, the standard deviation of the time averaged solids volume fraction differs from the fine grid simulation up to 50% in the gas-inflow area, the formation of distinct bubbles is recovered by the coarse grid simulation applying β_K, β_E, and β_{CL}. This is also observed from snapshots of the solids volume fraction, ϵ_s, in Figure 7. Obviously, while β_K, β_E, and β_{CL} deliver similar bubble patterns compared to the filtered fine grid simulation (Figure 7b) $\boldsymbol{\beta}_P$ (Figure 7d), β_P (Figure 7e), and β_{IS} (Figure 7h) reveal less distinct bubbles. It is noteworthy that β_{IS} and β_P reveal less pronounced bubbles than $\boldsymbol{\beta}_P$, while all of these modifications are derived from similar filtering approaches. In contrast to β_{IS} and β_P, which directly stem from filtering the drag force, $\boldsymbol{\beta}_P$ includes a second filter operation, which dynamically adapts the drag modification by introducing a subgrid drift velocity. Note that accounting for the subfilter stresses in the case of β_{IS} does not reveal more distinct bubbles than in the case of β_P ($\equiv \beta_{IS}$, compare with Figure 3). To conclude, it is observed that slip-velocity dependent drag modifications (β_K, β_E, β_{CL}) show as distinct bubbles as received from the reference simulation while ignoring the influence of the slip-velocity on H_D appears to smooth out the bubble edges (β_{IS}, β_P). $\boldsymbol{\beta}_P$ accounts for the slip-velocity implicitly by the second filter operation (Eq. 28) giving moderately pronounced bubbles.

Bubble Size, Number Density, and Rise Velocity. The results presented in the last subsection reveal that the different drag modifications deliver either distinct or less developed bubbles. Additionally, we may ask whether the coarse grid simulations are able to predict the mean bubble diameters, the bubble density, and the bubble rise velocity sufficiently. Thus, we evaluate the bubble properties using digital image analysis of the volume fraction maps of the center plane. The methodology follows the procedure presented by Li et al.[33] and Busciglio et al.[107] In a first step, the solid fractions are exported to a grayscale map and then converted to binary images by applying a constant grayscale threshold of t_b=0.5ϵ_s^{max}. After thresholding self-contained areas A_b with $d_b=\sqrt{4A_b/\pi} > \Delta_c$ are detected as bubbles, where valid area-centroids are limited to values between 0.05h_0 and h_0. This procedure eliminates on the one hand, all small bubbles close to the distributor plate, which tend to merge very quickly. Conversely, all erupting bubbles are excluded as soon as they have an open connection to the void section above the bed. In a second processing step, the identified bubbles are matched between two consecutive time steps in the sense of a Lagrangian object tracking.[108] It has to be

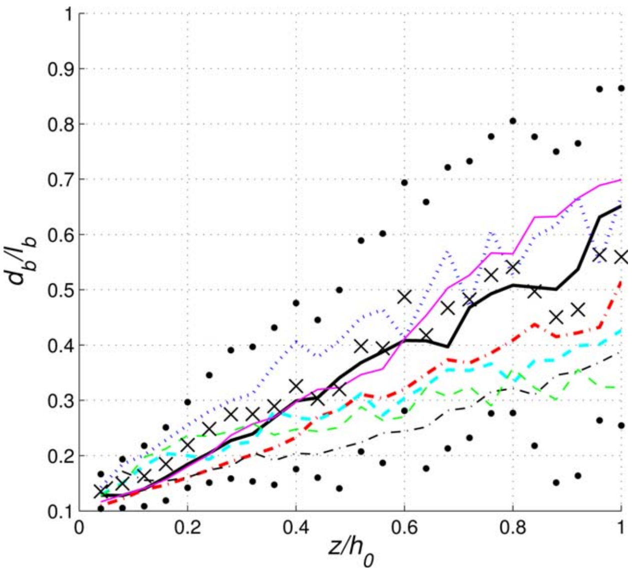

Figure 8. Dimensionless mean bubble diameter as a function of the normalized height z/h_0 for $W_g^{in}=0.21$ m s^{-1} and $\Delta_c=64d_s$ (sampling time is 10 s). l_b (=150 mm) denotes the length of the bed. The lines and symbols have the same meaning as in Figure 5.

The points indicate the spread of the bubble size obtained from the fine grid simulation. [Color figure can be viewed in the online issue, which is available at wileyonlinelibrary.com.]

noted that we determine the bubble behavior received from the fine grid simulation directly without an additional filtering operation.

In Figure 8, the corresponding dimensionless mean bubble diameter as a function of the normalized height z/h_0 is plotted. Remarkably, each drag modification is in fairly good agreement with the bubble size obtained from the fine grid simulation, that is, the increasing bubble diameter with decreasing hydrostatic pressure. β_{IS}, β_{P}, and $\boldsymbol{\beta}_{\mathrm{P}}$, which show less distinct bubbles than observed in the fine grid simulation, slightly underestimate the mean bubble diameter in the upper region of the bed. It is interesting to note that even the homogenous drag correlation β_{WY} yields the bubble diameter appropriately, that is, within the spread of the fine grid simulation. However, in the case of β_{IS}, β_{P}, $\boldsymbol{\beta}_{\mathrm{P}}$, and β_{WY} the value of the bubble threshold t_{b} appears to have a significant influence on the bubble statistics. Nevertheless, all coarse grid simulations yield a fairly good estimate of the mean bubble sizes with height.

Figure 9 shows the bubble number density as a function of the bubble diameter. All the drag modifications yield quite similar bubble distributions and are in fairly good agreement with the fine grid solution. However, below $z/h_0=0.1$ small bubbles of size $\mathcal{O}(\Delta_c)$ prevail in the case of the fine grid (Figure 7a) and, therefore, the coarse grid simulations underestimate the amount of bubbles near the distributor plate. This, in turn, gave indication of a grid limit for the smallest resolved bubble by the coarse mesh, which is also supported by Figure 9 yielding a considerable underestimation of the amount of bubbles with $d_{\mathrm{b}} < 0.2b \approx 2\Delta_{\mathrm{c}}$.

The bubble rise velocity u_{b} in a freely bubbling fluidized bed is usually correlated to the bubble diameter by[109]

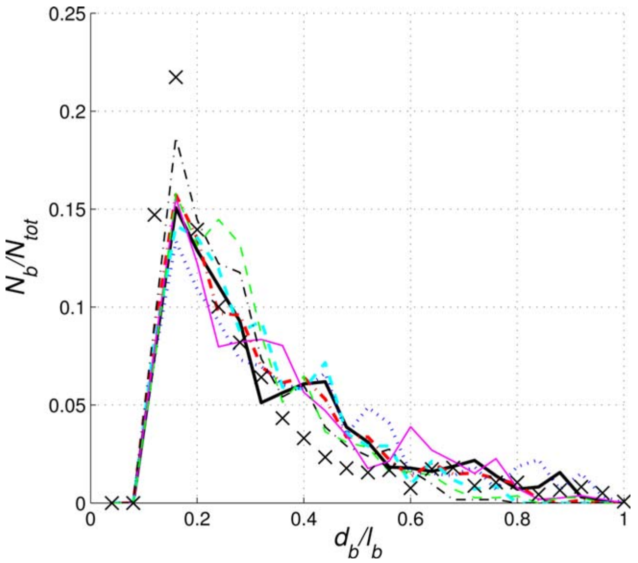

Figure 9. Normalized bubble number density as a function of the normalized mean bubble diameter d_b/b for $W_g^{in}=0.21$ m s^{-1} and $\Delta_c=64d_s$ (sampling time is 10 s). l_b (=150 mm) denotes the length of the bed.

The lines and symbols have the same meaning as in Figure 5. [Color figure can be viewed in the online issue, which is available at wileyonlinelibrary.com.]

$$u_{\mathrm{b}}=\psi\left(W_{\mathrm{g}}^{\mathrm{in}}-U_{\mathrm{g}}^{\mathrm{mf}}\right)+C\sqrt{gd_{\mathrm{b}}} \tag{52}$$

where different values between 0.5 and 1 have be proposed for the constant C. $U_{\mathrm{g}}^{\mathrm{mf}}$ denotes the superficial gas velocity at minimum fluidization conditions (cf. Table 2). In the case

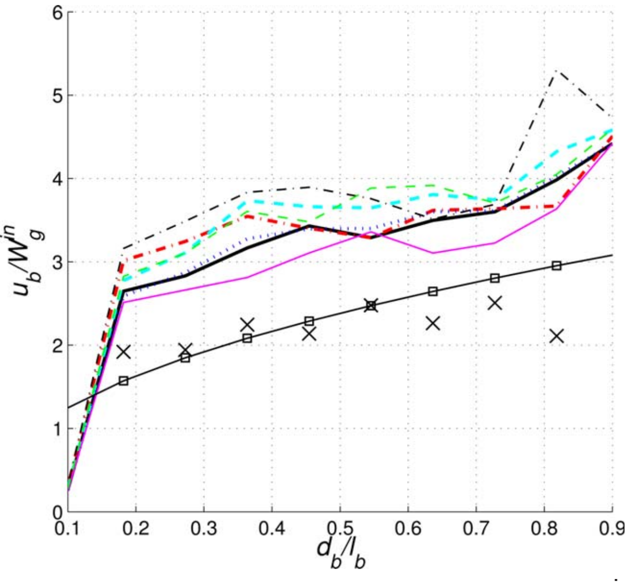

Figure 10. Dimensionless bubble rise velocity u_b/W_g^{in} as a function of the normalized bubble diameter d_b/b for $W_g^{in}=0.21$ m s^{-1} and $\Delta_c=64d_s$ (sampling time is 10 s). l_b (=150 mm) denotes the length of the bed.

The lines and symbols have the same meaning as in Figure 5. □ indicates Eq. 52 with $\psi=0.65$ and $C=0.5$. [Color figure can be viewed in the online issue, which is available at wileyonlinelibrary.com.]

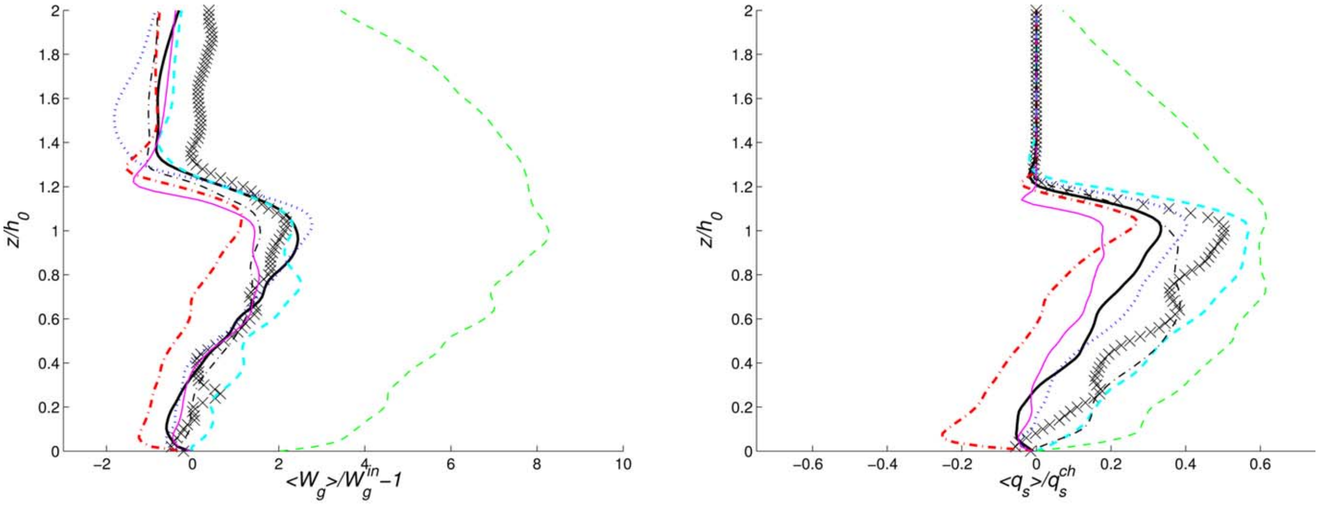

(a) (b)

Figure 11. Axial profiles of (a) the time averaged dimensionless superficial gas velocity in vertical direction, $\langle W_g \rangle / W_g^{in} - 1$ and (b) of the time averaged dimensionless particle mass flux in vertical direction, $\langle q_s \rangle / q_s^{ch}$, for $W_g^{in} = 0.21$ m s^{-1} and $\Delta_c = 64 d_s$ (the averaging time is 10 s).

The lines and symbols have the same meaning as in figure 5. Note the results of the fine grid simulation are displayed on the coarse grid by applying a box filter with filter length Δ_c. [Color figure can be viewed in the online issue, which is available at wileyonlinelibrary.com.]

of pseudo-2-D bubbling fluidized beds Mudde et al.[110] and Laverman et al.[108] suggested that using $C \approx 0.5$ gives fairly good agreement with experimental data. Especially, for high bed aspect ratios C appears to be independent of the bed width.[108] The value of the visual flow rate ψ, which has been determined by Hilligardt and Werther[111] for bed aspect ratios up to 2 to be approximately 0.65. We, therefore, compare the computed bubble rise velocities with Eq. 68 using $\psi = 0.65$ and $C = 0.5$. It has to be noted that we exclude bubble rise velocities from the statistics exceeding a maximum rise velocity, which is set to five times the bubble velocity u_b as obtained from Eq. 52 with $d_b = l_b$, where l_b ($=150$ mm) denotes the length of the bed.

Figure 10 reveals that the fine grid simulation shows fairly good agreement with Eq. 52. However, each coarse grid simulation considerably overestimates the rise velocity of the bubbles, although the size of the bubbles is consistent with the fine grid simulation. The raw data (not shown here) suggests that primarily the rise velocity of the larger bubbles is substantially overpredicted by the coarse grid simulations. This, in turn, implies that the countercurrently downflowing layer of particles around these larger bubbles[112] is not

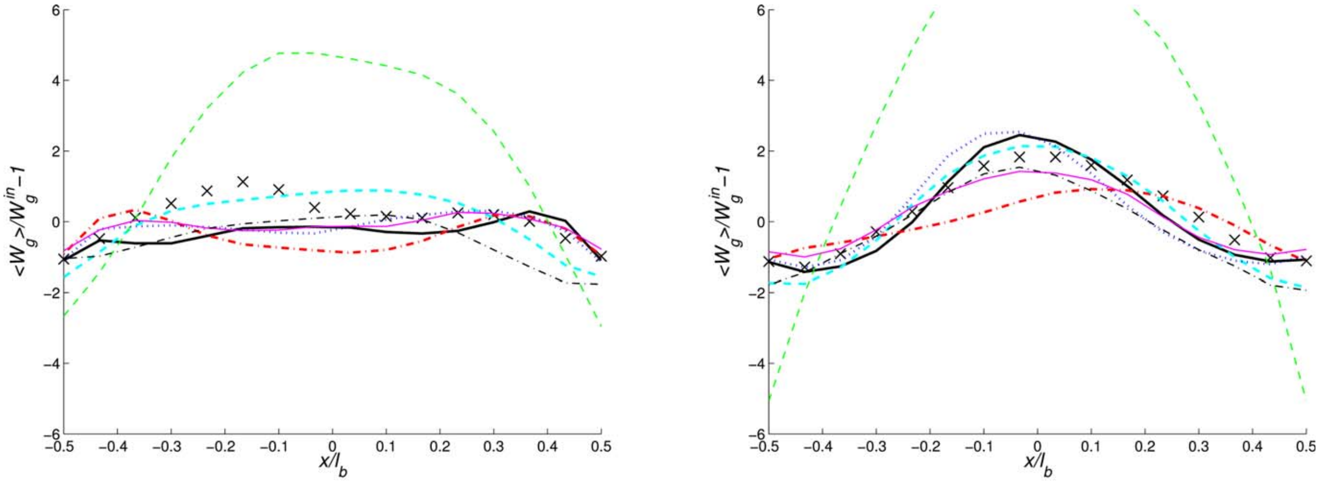

(a) (b)

Figure 12. Horizontal profiles in the middle plane of the time averaged dimensionless superficial gas velocity in vertical direction, $\langle W_g \rangle / W_g^{in} - 1$, for $W_g^{in} = 0.21$ m s^{-1} and $\Delta_c = 64 d_s$ (the averaging time is 10 s).

The lines and symbols have the same meaning as in Figure 5. Note the results of the fine grid simulation are displayed on the coarse grid by applying a box filter with filter length Δ_c. l_b ($=150$ mm) denotes the length of the bed. [Color figure can be viewed in the online issue, which is available at wileyonlinelibrary.com.]

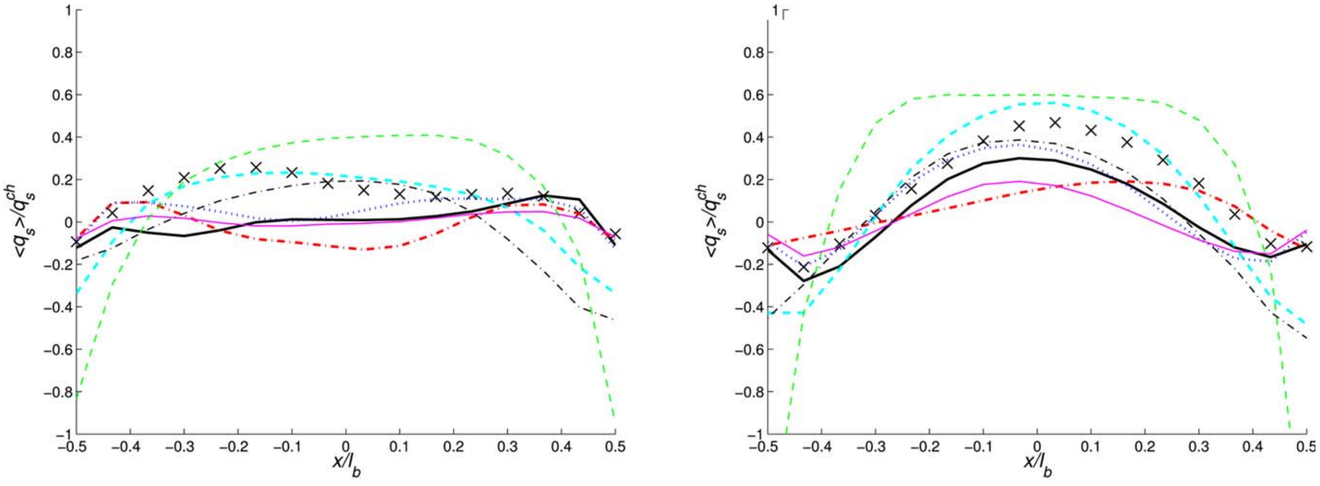

(a) (b)

Figure 13. Horizontal profiles in the middle plane of the time averaged dimensionless particle mass flux in vertical direction, $\langle q_{\rm s}\rangle/q_{\rm s}^{\rm ch}$, for $W_{\rm g}^{\rm in}=0.21$ m s^{-1} and $\Delta_{\rm c}=64d_{\rm s}$ (the averaging time is 10 s).

The lines and symbols have the same meaning as in Figure 5. Note the results of the fine grid simulation are displayed on the coarse grid by applying a box filter with filter length $\Delta_{\rm c}$. $l_{\rm b}$ (=150 mm) denotes the length of the bed. [Color figure can be viewed in the online issue, which is available at wileyonlinelibrary.com.]

resolved adequately supporting the demand of subgrid stress closures at volume fractions near the closest packing. Interestingly, the computed bubble rise velocity hardly depends on the drag modification.

Superficial Gas Flow. Figures 11a and 12 compare the axial and horizontal profiles of the time averaged dimensionless superficial gas velocities. The figures show that the coarse grid superficial gas velocities show same behavior as the fine grid simulation for all drag modifications in the case of $z/h_0 < 1$. Especially, in areas with higher voidage, that is, in the center region of the fluidized bed, higher-superficial gas velocities are observed, which are up to three times higher than the incoming superficial gas velocity. In the side regions, a countercurrent gas flow establishes to comply mass conservation, which is equally detected by the coarse grid simulations. The application of the homogenous drag correlation $\beta_{\rm WY}$, however, fails to predict the gas flow in the fluidized bed.

Particle Mass Flux. Figures 11b and 13 show the variations of the corresponding dimensionless solids mass flux, which is made dimensionless using a characteristic solid flux, $q_{\rm s}^{\rm ch}=\epsilon_{\rm s}^{\rm max}\,\rho_{\rm s}u_{\rm t}$.[60] Similar to the fine grid case, the coarse grid simulations yield rising particles in the center of the bed and slowly downward flowing particles in the dense side region. However, the particle phase mass flux is on the one hand, underestimated by $\beta_{\rm K}$, $\boldsymbol{\beta}_{\rm P}$, $\beta_{\rm E}$ and $\beta_{\rm CL}$ and on the other hand, correctly estimated by $\beta_{\rm P}$, $\beta_{\rm IS}$. The homogenous drag law $\beta_{\rm WY}$ yields a considerable overestimation of $\langle q_{\rm s}\rangle/q_{\rm s}^{\rm ch}$. Thus, Figures 11b and 13 indicate that the solids phase velocity is as well underestimated by $\beta_{\rm K}$ and $\beta_{\rm CL}$ because the time averaged solids volume fraction is in good agreement with the fine grid results for these drag modifications. In contrast, $\beta_{\rm IS}$ appears to compute the solids mass flux more precisely and, therefore, predicts the correct slip velocity. As before, although $\beta_{\rm WY}$ reveals the correct direction of the particle flux, its value is considerably overestimated compared to the fine grid case.

High-superficial gas velocity: $W_g^{in}=0.63ms^{-1}$

Particle Volume Fraction. Figure 14 compares the axial time-averaged profiles of the solids volume fraction, $\epsilon_{\rm s}$, and its standard deviation, σ_ϵ, for $W_{\rm g}^{\rm in}=0.63$ m s^{-1}. Similar to the $W_{\rm g}^{\rm in}=0.21$ m s^{-1} case the application of the homogenous drag coefficient $\beta_{\rm WY}$ yields a considerably overestimated bed expansion. Additionally, the $\beta_{\rm WY}$-results do not reflect the pronounced bubbling and slugging of the bed, respectively (see also Figures 15, 16a, b, and i). The figure highlights that the different subgrid drag closures give similar trends as in the case of $W_{\rm g}^{\rm in}=0.21$ m s^{-1}. While $\beta_{\rm P}$ overestimates the bed expansion and does not preserve bubbling (Figures 16e and h), $\beta_{\rm E}$ slightly underestimates the bed expansion but delivers sharp distinct bubbles (Figure 16e). In contrast to the prior case ($W_{\rm g}^{\rm in}=0.21$ m s^{-1}), the drag modification $\beta_{\rm K}$ slightly underpredicts the bed expansion which is a consequence of the considerable decrease of $H_{\rm d}^{\rm K}$ with increasing particle slip. $\beta_{\rm CL}$, $\boldsymbol{\beta}_{\rm P}$, $\beta_{\rm E}$, and $\beta_{\rm K}$ (Figures 14c–d and e–f) overestimate the solids volume fraction directly above the gas feed, which may be attributed to neglecting inflow effects [29,60] by the different models and the contribution of the subgrid particle stresses. In particular, in the case of $\beta_{\rm E}$ and $\beta_{\rm CL}$ it is not reasonable that larger clusters are observed directly above the distributor plate. In contrast to $\beta_{\rm P}$, accounting for the contribution of the subgrid stresses in the case of $\beta_{\rm IS}$ yields a fairly good estimate of the particle distribution.

At the top of the bed, Figures 14a and 16a report the entrainment of small particle clusters with a diameter of $\mathcal{O}(\Delta_{\rm c})$, which is only observed in the case of $\boldsymbol{\beta}_{\rm P}$ and $\beta_{\rm IS}$ adequately. Despite such a deficiency, $\beta_{\rm CL}$ also reveals a fairly good estimate of the bed expansion. Furthermore, the standard deviations of $\langle\epsilon_{\rm s}\rangle$ indicate appropriate bubbling behavior in the case of $\boldsymbol{\beta}_{\rm P}$, $\beta_{\rm E}$, $\beta_{\rm K}$, and $\beta_{\rm CL}$ similar to the $W_{\rm g}^{\rm in}=0.21$ m s^{-1}. This is also deduced from Figure 16.

Figure 15 reports bubble aggregation in the center of the bed in the case of the fine grid simulation, which is also

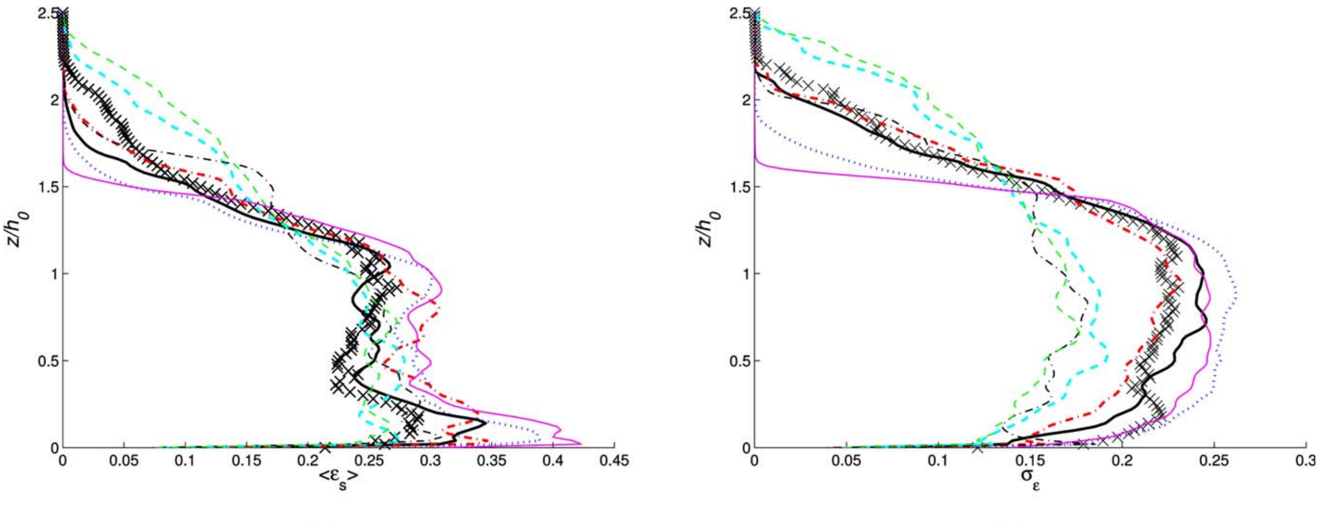

(a) (b)

Figure 14. Axial profiles of the time averaged solids volume fraction, $\langle \epsilon_s \rangle$, and its standard deviation, σ_ϵ, for $W_g^{in}=0.63$ m s^{-1} and $\Delta_c=64d_s$ (the averaging time is 10 s).

The lines and symbols have the same meaning as in Figure 5. Note the results of the fine grid simulation are displayed on the coarse grid by applying a box filter with filter length Δ_c. [Color figure can be viewed in the online issue, which is available at wileyonlinelibrary.com.]

observed from coarse grid results. Again the results indicate the necessity of wall corrections.

Bubble Size, Number Density, and Rise Velocity. Figure 17 compares the dimensionless mean bubble diameter as a function of the dimensionless height z/h_0. The bubble sizes are predicted appropriately by all coarse grid simulations in the lower part of the bed. The decreasing bubble diameter with increasing height above $z/h_0 \approx 0.7$ is attributed to the bursting of larger bubbles and slugs at the top of the bed, while smaller bubbles persist. However, these small bubbles are detected very infrequently by the coarse grid simulations in contrast to the reference case.

Figure 18 reports the bubble number density as a function of the dimensionless bubble diameter. Remarkably, the coarse grid simulations reveal a fairly good measure of bubble number density. However, the amount of small bubble directly above gas feed, that is, $\mathcal{O}(d_b) \gtrsim \mathcal{O}(\Delta_c)$, is underestimated using coarse grids.

In contrast to $W_g^{in}=0.21$ m s^{-1}, Figure 19 emphasizes that each coarse grid simulation is able to predict the bubble (slug) rise velocities as a function of the dimensionless bubble diameter. Figures 7 and 16 reveal that in the case of low superficial gas velocities typical bubbles with a circular cap and a downstream wake dominate; whereas, in the case of

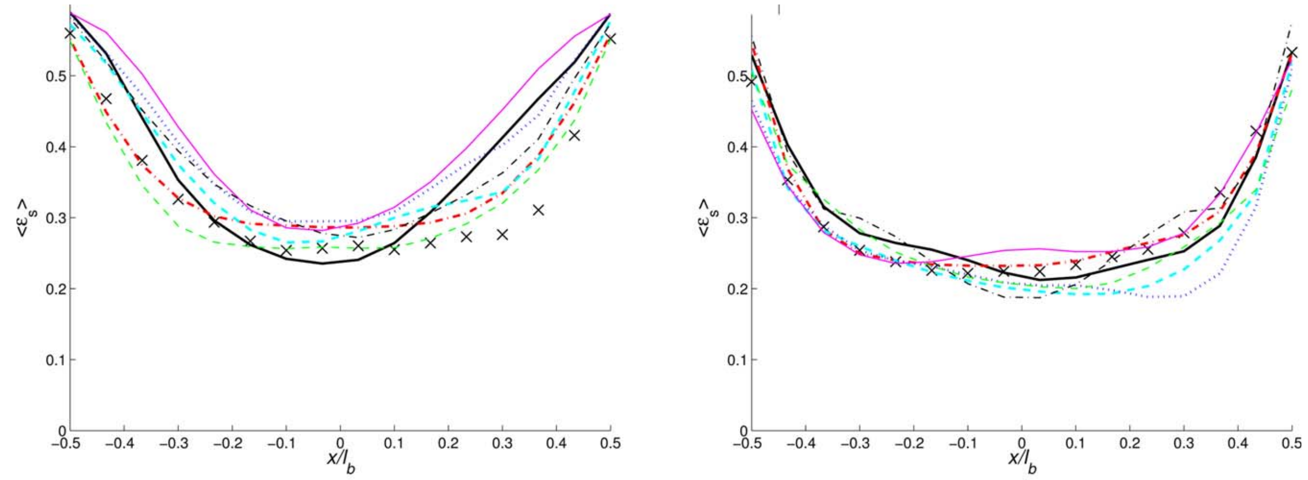

(a) (b)

Figure 15. Horizontal profiles in the middle plane of the time averaged solids volume fraction, $\langle \epsilon_s \rangle$, for $W_g^{in}=0.63$ m s^{-1} and $\Delta_c=64d_s$ (the averaging time is 10 s).

The lines and symbols have the same meaning as in Figure 5. Note the results of the fine grid simulation are displayed on the coarse grid by applying a box filter with filter length Δ_c. l_b (=150 mm) denotes the length of the bed. [Color figure can be viewed in the online issue, which is available at wileyonlinelibrary.com.]

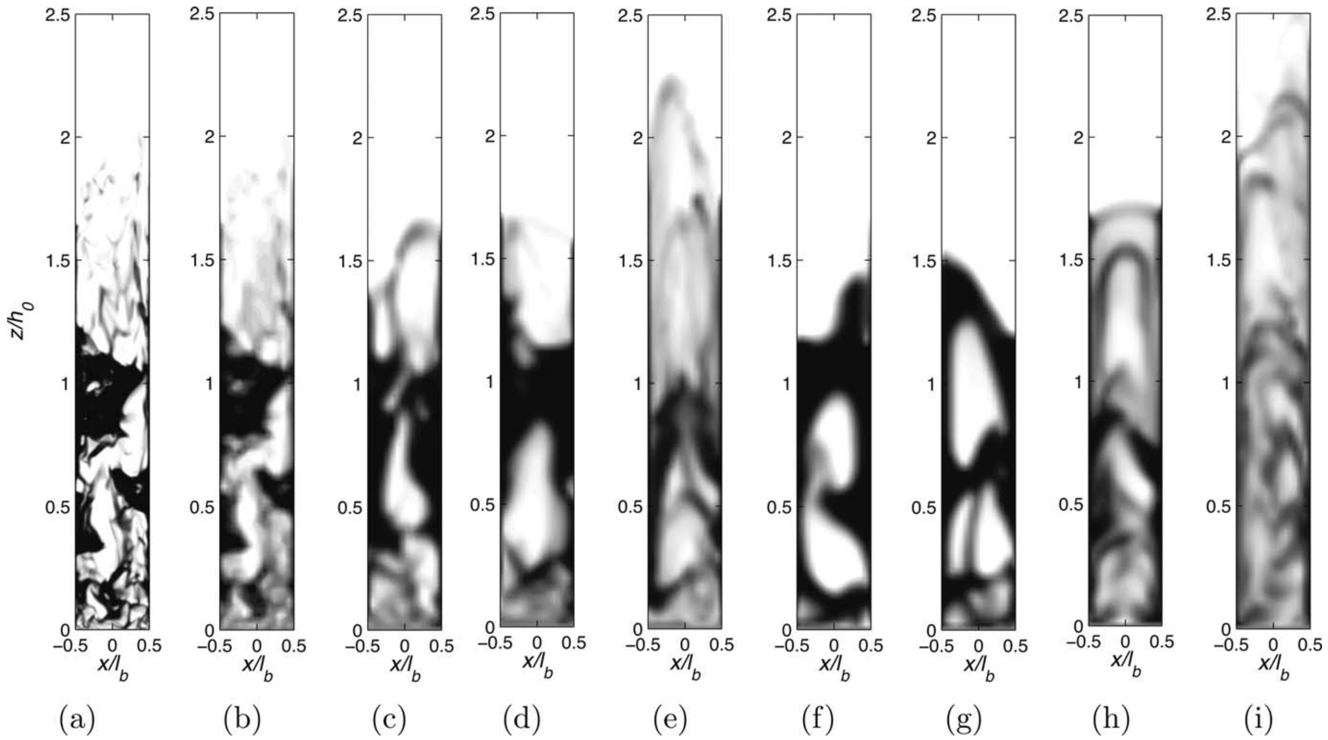

(a) (b) (c) (d) (e) (f) (g) (h) (i)

Figure 16. Snapshots of the solids volume fraction, ϵ_s, at t = 10 s for W_g^{in} =0.63 m s^{-1} (white: ϵ_s=0; black: $\epsilon_s=\epsilon_s^{\max}$). (a) fine grid, (b) fine grid with applied box filter with $l_\Delta=\Delta$, (c) coarse grid using β_{CL} (Eq. 51), (d) coarse grid using β_P (Eq. 26), (e) coarse grid using β_P (K = 1) (Eq. 27), (f) coarse grid using β_K (Eq. 16), (g) coarse grid using β_E (Eq. 9), (h) coarse grid using β_{IS} (Eq. 19), (i) coarse grid using β_{WY} (Eq. 58). l_b (=150 mm) denotes the length of the bed.

The figure shows distinct bubbles for β_P, β_{CL}, β_K, β_E and blurred bubbles for β_P (K = 1), β_{IS} and β_{WY}.

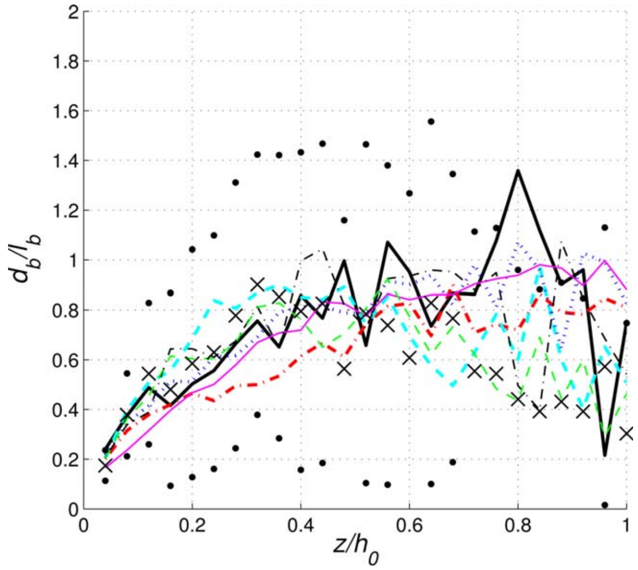

Figure 17. Dimensionless mean bubble diameter as a function of the normalized height z/h_0 for W_g^{in} =0.63 m s^{-1} and Δ_c=64d_s (sampling time is 10 s). l_b (=150 mm) denotes the length of the bed.

The lines and symbols have the same meaning as in Figure 5. The points indicate the spread of the bubble size obtained from the fine grid simulation. [Color figure can be viewed in the online issue, which is available at wileyonlinelibrary.com.]

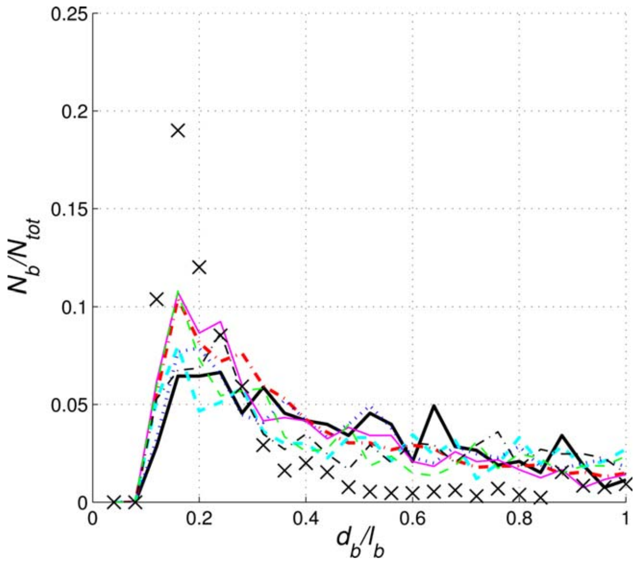

Figure 18. Normalized bubble number density as a function of the normalized mean bubble diameter d_b/b for W_g^{in} =0.63 m s^{-1} and Δ_c=64d_s (sampling time is 10 s). l_b (=150 mm) denotes the length of the bed.

The lines and symbols have the same meaning as in Figure 5. [Color figure can be viewed in the online issue, which is available at wileyonlinelibrary.com.]

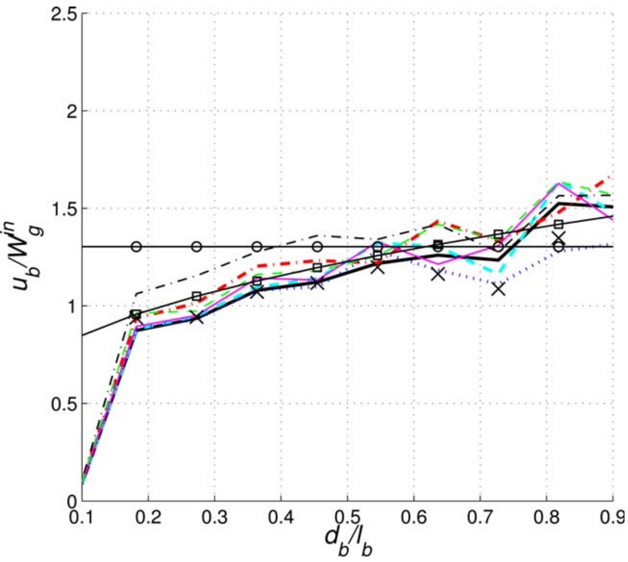

Figure 19. Dimensionless bubble rise velocity u_b/W_g^{in} as a function of the normalized bubble diameter d_b/b for $W_g^{in}=0.63$ m s^{-1} and $\Delta_c=64d_s$ (sampling time is 10 s). l_b (=150 mm) denotes the length of the bed.

The lines and symbols have the same meaning as in Figure 5. □ indicates Eq. 68 with $\psi=0.65$ and $C=0.5$; ○ represents the slug rise velocity[113] $u_{sl}=W_g^{in}-U_g^{mf}+\varphi\sqrt{gb/2}$ with $\varphi=0.48$. [Color figure can be viewed in the online issue, which is available at wileyonlinelibrary.com.]

high-superficial gas velocities larger bubble has the form of long vertical slugs with high-aspect ratios.

Superficial Gas Flow and Particle Mass Flux. The profiles of the dimensionless superficial gas velocities and the dimensionless particle mass fluxes (not shown here) show similar trends as in the case of $W_g^{in}=0.21$ m s^{-1}. That is the strong upward current of gas in the center and a countercurrent gas flow in the side regions of the bed. Rising particles in the center of the bed and slowly downward moving particles in the dense side region are also observed. This is also consistent with the reference simulation.

Conclusions

We have introduced a new closure for the heterogeneity index H_d, that is the correction of a homogenous drag correlation to account for subgrid structures. Its derivation is based on the assumption about the formation of clusters. In contrast to EMMS, which is also fundamentally based on the cluster concept, we distinguish between resolved and unresolved clusters. Furthermore, we assumed that the solids volume within the dilute phase is negligibly small leading to a closed set of equation for the heterogeneity index.

We have also presented a comparative study of the drag correlations of the groups of EMMS,[26] Kuipers (Wang et al.[27]), Sundaresan (Igci et al.[38,39]), Simonin (Parmentier et al.[28]), the presented relation and the homogenous drag law of Wen and Yu,[80] which have been applied to a coarse grid simulation of a bubbling fluidized bed of fine glass particles (Geldart type B) at two different superficial gas velocities ($W_g^{in}/u_t=0.21$ and $W_g^{in}/u_t=0.63$). The results are discussed with respect to fine grid reference simulations. This comparative study reveals that:

(a) Applying a homogenous drag law, which ignores unresolved subgrid structures, fails to predict the hydrodynamics of the bubbling fluidized bed using a coarse mesh.

(b) Applying one of the discussed subgrid drag modifications reveals the main features of the gas-particle flow in the bubbling fluidized bed and each subgrid drag modification estimates the bed expansion adequately (with a maximum error of ±10%) for both superficial gas velocities. However, the drag corrections of Parmentier et al.[28] considering the dynamic adjustment procedure, EMMS[26] and Wang et al.[27] tend to underestimate the mean voidage in the center of the bed, while the remaining subgrid modifications yield fairly good agreement of the particle distribution with the fine grid results (Figures 5, 6, 14 and 15).

(c) A drag modification is expected to show an appropriate functional dependence on the grid spacing to reveal grid-independent solutions.

(d) The subgrid modifications can be classified into the models, which yield sharp distinct bubbles, and the models, which return smooth blurred bubbles. The results indicate that ignoring the impact of the slip-velocity on the drag modification yields less distinct bubbles than slip velocity dependent modifications. For example, recently considerable effort has been made to account for the slip-velocity in filtered subgrid drag modifications.[114]

(e) The bubble size and the bubble number density are estimated suitably by the investigated subgrid drag closures.

(f) While in the case of low superficial gas velocities, the bubble rise velocity is significantly overestimated by these closures, the slug rise velocity is in quite good agreement with the fine grid simulation in the case of high-superficial gas velocities, which may be attributed to the higher ratio between drag and frictional stresses in the latter case. Thus, the unresolved part of the frictional particle stresses has to be considered in bubbling fluidized beds.

(g) The contribution of the unresolved collisional particle stresses considerably improves the prediction of the particle distribution.

(h) Compared to the fine grid simulation, the computational demand is reduced by approximately two orders of magnitude using the coarse grid for equal time step sizes. Coarse meshes, however, allow larger time steps that additionally improve the computational efficiency by approximately one order of magnitude in our study.

To conclude, this study demonstrates that the discussed subgrid drag modifications apply well to the coarse grid simulation of a bubbling fluidized bed of fine particles. However, several tasks remain. First, it is necessary to study further the impact of the unresolved part of the particle stresses on the hydrodynamics of a bubbling fluidized bed, especially in the frictional regime. These may have a considerable impact on the computed bubble rise velocities. Second, the models should also be tested at even coarser meshes, which directly connect to the assumption of a homogenous particle distribution within clusters in the case of the presented model. Finally, the general validity of the models must be further studied. These will be discussed in future publications.

Acknowledgments

This work was funded by the Christian-Doppler Research Association, the Austrian Federal Ministry of Economy, Family and Youth, and the Austrian National Foundation for Research, Technology and Development. The authors would like to thank Stefan Radl for many useful discussions and helpful comments.

Literarure Cited

1. Rapagnà S, Jand N, Kiennemann A, Foscolo PU. Steam-gasification of biomass in a fluidised-bed of olivine particles. *Biomass Bioenergy.* 2000;19:187–197.
2. Papadikis K, Bridgwater A, Gu S. CFD modelling of the fast pyrolysis of biomass in fluidised bed reactors, Part A: Eulerian computation of momentum transport in bubbling fluidised beds. *Chem Eng Sci.* 2008;63:4218–4227.
3. Papadikis K, Gu S, Bridgwater A. CFD modelling of the fast pyrolysis of biomass in fluidised bed reactors. Part B: Heat, momentum and mass transport in bubbling fluidised beds. *Chem Eng Sci.* 2009; 64:1036–1045.
4. Xue Q, Heindel TJ, Fox RO. A CFD model for biomass fast pyrolysis in fluidized-bed reactors. *Chem Eng Sci.* 2011;66:2440–2452.
5. Hatzantonis H, Yiannoulakis H, Yiagopoulos A, Kiparissides C. Recent developments in modeling gas-phase catalyzed olefin polymerization fluidized-bed reactors: The effect of bubble size variation on the reactor's performance. *Chem Eng Sci.* 2000;55:3237–3259.
6. Fernandes FAN, Lona LMF. Heterogeneous modeling for fluidized-bed polymerization reactor. *Chem Eng Sci.* 2001;56:963–969.
7. Rokkam RG, Fox RO, Muhle ME. Computational fluid dynamics and electrostatic modeling of polymerization fluidized-bed reactors. *Powder Technol.* 2010;203:109–124.
8. Lyngfelt A, Leckner B, Mattisson T. A fuidized-bed combustion process with inherent CO2 separation; application of chemical-looping combustion. *Chem Eng Sci.* 2001;56:3101–3113.
9. Gilliland ER, Mason EA. Gas and Solid Mixing in Fluidized Beds. *Ind Eng Chem.* 1949;41:1191–1196.
10. Mickley HS, Trilling CA. Heat Transfer Characteristics of Fluidized Beds. *Ind Eng Chem.* 1949;41:1135–1147.
11. Mickley HS, Fairbanks DF. Mechanism of heat transfer to fluidized beds. *AIChE J.* 1955;1:374–384.
12. Syamlal M, Rogers W, O'Brien TJ. MFIX documentation theory guide, Technical note. Technical report, U.S. Department of Energy, Office of Fossil Energy: Morgantown, West Virginia, 1993.
13. Enwald H, Peirano E, Almstedt AE. Eulerian two-phase flow theory applied to fluidization. *Int J Multiphase Flow.* 1996;22:21–66.
14. van Wachem BGM, Schouten JC, Krishna R, van den Bleek CM. Validation of the Eulerian simulated dynamic behaviour of gas-solid fluidised beds. *Chem Eng Sci.* 1999;54:2141–2149.
15. van Wachem BGM, Schouten JC, van den Bleek CM, Krishna R, Sinclair JL. Comparative analysis of CFD models of dense gas-solid systems. *AIChE J.* 2001;47:1035–1051.
16. Almuttahar A, Taghipour F. Computational fluid dynamics of high density circulating fluidized bed riser: study of modeling parameters. *Powder Technol.* 2008;185:11–23.
17. Reuge N, Cadoret L, Coufort-Saudejaud C, Pannala S, Syamlal M, Caussat B. Multifluid Eulerian modeling of dense gas-solids fluidized bed hydrodynamics: influence of the dissipation parameters. *Chem Eng Sci.* 2008;63:5540–5551.
18. Passalacqua A, Fox RO. Implementation of an iterative solution procedure for multi-fluid gas-particle flow models on unstructured grids. *Powder Technol.* 2011;213:174–187.
19. Du W, Bao X, Xu J, Wei W. Computational fluid dynamics (CFD) modeling of spouted bed: assessment of drag coefficient correlations. *Chem Eng Sci.* 2006;61:1401–1420.
20. Gryczka O, Heinrich S, Deen NG, Kuipers JAM, Mörl L. Three-Dimensional computational fluid dynamics modeling of a prismatic spouted bed. *Chem Eng Technol.* 2009;32:470–481.
21. Gryczka O, Heinrich S, Deen NG, van Sint Annaland M, Kuipers JAM, Mörl L. CFD modeling of a prismatic spouted bed with two adjustable gas inlets. *Can J Chem Eng.* 2009;87:318–328.
22. Chen XZ, Shi DP, Gao X, Luo ZH. A fundamental CFD study of the gas-solid flow field in fluidized bed polymerization reactors. *Powder Technol.* 2011;205:276–288.
23. Schneiderbauer S, Aigner A, Pirker S. A comprehensive frictional-kinetic model for gas-particle flows: analysis of fluidized and moving bed regimes. *Chem Eng Sci.* 2012;80:279–292.
24. Schneiderbauer S, Pirker S. CFD study of a single-spout pseudo-2D bed: the impact of the solids wall boundary conditions. In: Jha MK, Lazard M, Zaharim A, Sopian K, editors. Proceedings of the 9th WSEAS International Conference on Fluid Mechanics (FLUIDS '12), Harvard, Cambridge, MA: WSEAS, 2012:150–155.
25. Goniva C, Kloss C, Deen NG, Kuipers JAM, Pirker S. Influence of rolling friction on single spout fluidized bed simulation. *Particuology.* 2012;10:582–591.
26. Lu B, Wang W, Li J. Searching for a mesh-independent sub-grid model for CFD simulation of gas-solid riser flows. *Chem Eng Sci.* 2009;64:3437–3447.
27. Wang J, van der Hoef MA, Kuipers JAM. Coarse grid simulation of bed expansion characteristics of industrial-scale gas-solid bubbling fluidized beds. *Chem Eng Sci.* 2010;65:2125–2131.
28. Parmentier JF, Simonin O, Delsart O. A functional subgrid drift velocity model for filtered drag prediction in dense fluidized bed. *AIChE J.* 2012;58:1084–1098.
29. Igci Y, Pannala S, Benyahia S, Sundaresan S. Validation studies on filtered model equations for gas-particle flows in risers. *Ind Eng Chem Res.* 2012;51:2094–2103.
30. Wang J, van der Hoef MA, Kuipers JAM. Why the two-fluid model fails to predict the bed expansion characteristics of Geldart A particles in gas-fluidized beds: a tentative answer. *Chem Eng Sci.* 2009; 64:622–625.
31. Benyahia S, Sundaresan S. Do we need sub-grid scale corrections for both continuum and discrete gas-particle flow models? *Powder Technol.* 2012;220:2–6.
32. Benyahia S. Fine-grid simulations of gas-solids flow in a circulating fluidized bed. *AIChE J.* 2012;58:3589–3592.
33. Li T, Grace J, Bi X. Study of wall boundary condition in numerical simulations of bubbling fluidized beds. *Powder Technol.* 2010;203: 447–457.
34. Mckeen T, Pugsley T. Simulation and experimental validation of a freely bubbling bed of FCC catalyst. *Powder Technol.* 2003;129: 139–152.
35. Makkawi YT, Wright PC, Ocone R. The effect of friction and inter-particle cohesive forces on the hydrodynamics of gas-solid flow: a comparative analysis of theoretical predictions and experiments. *Powder Technol.* 2006;163:69–79.
36. Gao J, Lan X, Fan Y, Chang J, Wang G, Lu C, Xu C. CFD modeling and validation of the turbulent fluidized bed of FCC particles. *AIChE J.* 2009;55:1680–1694.
37. Wang J. A review of eulerian simulation of geldart a particles in gas-fluidized beds. *Ind Eng Chem Res.* 2009;48:5567–5577.
38. Igci Y, Andrews AT, Sundaresan S, Pannala S, O'Brien T. Filtered Two-Fluid Models for Fluidized Gas-Particle Suspensions. *AIChE J.* 2008;54:1431–1448.
39. Igci Y, Sundaresan S. Constitutive models for filtered two-fluid models of fluidized gas-particle flows. *Ind Eng Chem Res.* 2011;50: 13190–13201.
40. Shuai W, Huilin L, Guodong L, Zhiheng S, Pengfei X, Gidaspow D. Modeling of cluster structure-dependent drag with Eulerian approach for circulating fluidized beds. *Powder Technol.* 2011;208:98–110.
41. Shuai W, Guodong L, Huilin L, Pengfei X, Yunchao Y, Gidaspow D. A cluster structure-dependent drag coefficient model applied to risers. *Powder Technol.* 2012;225:176–189.
42. Schneiderbauer S, Schellander D, Pirker S. A filtered frictional-kinetic model for gas-solid fluidized and moving beds. In: Witt PJ, editor. Proceedings of the 9th International Conference on CFD in the Minerals and Process Industries. Melbourne, Australia: CSIRO, 2012;7.
43. Koenigsdorff R, Werther J. Gas-solids mixing and flow structure modeling of the upper dilute zone of a circulating fluidized bed. *Powder Technol.* 1995;82:317–329.
44. Xu G, Li J. Multi-scale interfacial stresses in heterogeneous particle-fluid systems. *Chem Eng Sci.* 1998;53:3335–3339.
45. Agrawal K, Loezos PN, Syamlal M, Sundaresan S. The role of meso-scale structures in rapid gas-solid flows. *J. Fluid Mech.* 2001; 445:151–185.
46. Zhang DZ, VanderHeyden WB. The effects of mesoscale structures on the macroscopic momentum equations for two-phase flows. *Int J Multiphase Flow.* 2002;28:805–822.

47. Andrews AT, Loezos PN, Sundaresan S. Coarse-grid simulation of gas-particle flows in vertical risers. *Ind Eng Chem Res.* 2005;44: 6022–6037.
48. Milioli CC, Milioli FE. The Sub-grid Hydrodynamic Behavior of Accelerating Gas-solid Flows. In: Sinclair Curtis J, Balachandar S, editors. Proceedings of the 7th International Conference on Multiphase Flow, Tampa, Florida: University of Florida, 2010;9.
49. Milioli CC, Milioli FE. On the accuracy of two-fluid model predictions for a particular gas-solid riser flow. *Appl Math Model.* 2010; 34:684–696.
50. Li J, Kwauk M. Particle-Fluid Two-Phase Flow: The Energy-Minimization Multi-Scale Method. Beijing, China: Metallurgical Industry Press, 1994.
51. Liu M, Li J, Kwauk M. Application of the energy-minimization multi-scale method to gas-liquid-solid uidized beds. *Chem Eng Sci.* 2001;56:6805–6812.
52. Yang N, Wang W, Ge W, Li J. CFD simulation of concurrent-up gassolid flow in circulating fluidized beds with structure-dependent drag coefficient. *Chem Eng J.* 2003;96:71–80.
53. Wang W, Li J. Simulation of gas-solid two-phase flow by a multi-scale CFD approach – of the EMMS model to the sub-grid level. *Chem Eng Sci.* 2007;62:208–231.
54. Wang J, Ge W, Li J. Eulerian simulation of heterogeneous gas-solid flows in CFB risers: EMMS-based sub-grid scale model with a revised cluster description. *Chem Eng Sci.* 2008;63:1553–1571.
55. Nikolopoulos A, Atsonios K, Nikolopoulos N, Grammelis P, Kakaras E. An advanced EMMS scheme for the prediction of drag coefficient under a 1.2MWth CFBC isothermal flow–Part II: numerical implementation. *Chem Eng Sci.* 2010;65:4089–4099.
56. Nikolopoulos A, Papafotiou D, Nikolopoulos N, Grammelis P, Kakaras E. An advanced EMMS scheme for the prediction of drag coefficient under a 1.2MWth CFBC isothermal flow—Part I: numerical formulation. *Chem Eng Sci.* 2010;65:4080–4088.
57. Hong K, Wang W, Zhou Q, Wang J, Li J. An EMMS-based multi-fluid model (EFM) for heterogeneous gas-solid riser flows: Part I. Formulation of structure-dependent conservation equations. *Chem Eng Sci.* 2012;75:376–389.
58. Shi Z, Wang W, Li J. A bubble-based EMMS model for gas-solid bubbling fluidization. *Chem Eng Sci.* 2011;66:5541–5555.
59. Özel A, Parmentier JF, Simonin O, Fede P. A priori test of effective drag modeling for filtered two-fluid model simulation of circulating and dense gas-solid fluidized beds. In: Sinclair Curtis J, Balachandar S, editors. Proceedings of the 7th International Conference on Multiphase Flow, Tampa, Florida: 2010;7.
60. Igci Y, Sundaresan S. Verification of filtered two-fluid models for gas-particle flows in risers. *AIChE J.* 2011;57:2691–2707.
61. Werther J, Wein J. Expansion behavior of gas fluidized bed in the turbulent regime. *AIChE Symp Ser.* 1994;90:31–44.
62. Bokkers G, Laverman JA, van Sint Annaland M, Kuipers JAM. Modelling of large-scale dense gas-solid bubbling fluidised beds using a novel discrete bubble model. *Chem Eng Sci.* 2006;61:5590–5602.
63. Briongos JV, Sanchéz-Delgado S, Acosta-Iborra A, Santana D. A novel approach for modeling bubbling gas - solid fluidized beds. *AIChE J.* 2011;57:1733–1750.
64. da Cruz F, Emam S, Prochnow M, Roux JN, Chevoir F. Rheophysics of dense granular materials: discrete simulation of plane shear flows. *Phys Rev E.* 2005;72:021309.
65. Jop P, Forterre Y, Pouliquen O. A constitutive law for dense granular flows. *Nature.* 2006;441:727–730.
66. Pouliquen O, Cassar C, Jop P, Forterre Y, Nicolas M. Flow of dense granular material: towards simple constitutive laws. *J Stat Mech.* 2006;2006:P07020.
67. Forterre J, Pouliquen O. Flow of dense granular media. *Annu Rev Fluid Mech.* 2008;40:1–24.
68. Germano M, Piomelli U, Moin P, Cabot WH. A dynamic subgrid-scale eddy viscosity model. *Phys Fluids A.* 1991;3:1760–1765.
69. Lilly DK. A proposed modification of the Germano subgrid-scale closure method. *Phys Fluids A.* 1992;4:633–635.
70. Benyahia S. On the effect of subgrid drag closures. *Ind Eng Chem Res.* 2010;49:5122–5131.
71. Yang N, Wang W, Ge W, Wang L, Li J. Simulation of Heterogeneous Structure in a Circulating Fluidized-Bed Riser by Combining the Two-Fluid Model with the EMMS approach. *Ind Eng Chem Res.* 2004;43:5548–5561.
72. Anderson TB, Jackson R. Fluid mechanical description of fluidized beds. *Equations of motion. Ind Eng Chem Fundam.* 1967;6:527–539.
73. Ishii M. Thermo-fluid dynamic theory of two-phase flow. Collection de la Direction des Etudes et recherches d'Electricité de France. Paris: Eyrolles, 1975.
74. van Wachem BGM, Almstedt A. Methods for multiphase computational fluid dynamics. *Chem Eng J.* 2003;96:81–98.
75. Chapman S, Cowling TG. The Mathematical Theory of Non-uniform Gases, 3rd ed. New York: Cambridge University Press, 1970.
76. Lun CKK, Savage SB, Jeffrey DJ, Chepurniy N. Kinetic theories for granular flow: inelastic particles in Couette flow and slightly inelastic particles in a general flowfield. *J Fluid Mech.* 1984;140:223–256.
77. Rao KK, Nott PR. An Introduction to Granular Flow. Cambridge Series in Chemical Engineering. New York: Cambridge University Press, 2008.
78. Busciglio A, Vella G, Micale G, Rizzuti L. Analysis of the bubbling behaviour of 2D gas solid fluidized beds Part II. Comparison between experiments and numerical simulations via Digital Image Analysis Technique. *Chem Eng J.* 2009;148:145–163.
79. van der Hoef MA, van Sint Annaland M, Deen NG, Kuipers JAM. Numerical simulation of dense gas-solid fluidized beds: a multiscale modeling strategy. *Annu Rev Fluid Mech.* 2008;40:47–70.
80. Wen CY, Yu YH. Mechanics of fluidization. *Chem Eng Prog Symp Series.* 1966;62:100–111.
81. Zou B, Li H, Xia Y, Ma X. Cluster structure in a circulating fluidized bed. *Powder Technol.* 1994;78:173–178.
82. Li H, Zhu Q, Liu H, Zhou Y. The cluster size distribution and motion behavior in a fast fluidized bed. *Powder Technol.* 1995;84: 241–246.
83. Wei F, Yang GQ, Jin Y, Yu ZQ. The characteristics of cluster in a high density circulating fluidized bed. *Can J Chem Eng.* 1995;73: 650–655.
84. Tsuji Y, Tanaka T, Yonemura S. Cluster patterns in circulating fluidized beds predicted by numerical simulation (discrete particle model versus two-fluid model). *Powder Technol.* 1998;95:254–264.
85. Xu G, Kato K. Hydrodynamic equivalent diameter for clusters in heterogeneous gas-solid flow. *Chem Eng Sci.* 1999;54:1837–1847.
86. Li H. Multi-scale aggregation of particles in gas-solids fluidized beds. *China Particuol.* 2004;2:101–106.
87. Lu X, Li S, Du L, Yao J, Lin W, Li H. Flow structures in the downer circulating fluidized bed. *Chem Eng J.* 2005;73:23–31.
88. Jiradilok V, Gidaspow D, Damronglerd S, Koves WJ, Mostofi R. Kinetic theory based CFD simulation of turbulent fluidization of FCC particles in a riser. *Chem Eng Sci.* 2006;61:5544–5559.
89. Huilin L, Qiaoqun S, Yurong H, Yongli S, Ding J, Xiang L. Numerical study of particle cluster flow in risers with cluster-based approach. *Chem Eng Sci.* 2005;60:6757–6767.
90. Wang J, Ge W. Multi-scale analysis on particle-phase stresses of coarse particles in bubbling fluidized beds. *Chem Eng Sci.* 2006;61: 2736–2741.
91. Wang W, Lu B, Li J. Choking and flow regime transitions: simulation by a multi-scale CFD approach. *Chem Eng Sci.* 2007;62:814–819.
92. Lu B, Wang W, Li J, Wang X, Gao S, Lu W, Xu Y, Long J. Multi-scale CFD simulation of gas-solid flow in MIP reactors with a structure-dependent drag model. *Cheml Eng Sci.* 2007;62:5487–5494.
93. Qi H, Li F, Xi B, You C. Modeling of drag with the Eulerian approach and EMMS theory for heterogeneous dense gas-solid two-phase flow. *Chem Eng Sci.* 2007;62:1670–1681.
94. Zhang N, Lu B, Wang W, Li J. Virtual experimentation through 3D full-loop simulation of a circulating fluidized bed. *Particuology.* 2008;6:529–539.
95. Richardson JF, Zaki WN. Sedimentation and Fluidization. *Trans Inst Chem Eng.* 1954;32:35–53.
96. Ye M, Wang J, van der Hoef MA, Kuipers JAM. Two-fluid modeling of Geldart A particles in gas-fluidized beds. *Particuology.* 2008; 6:540–548.
97. Johnson PC, Jackson R. Frictional-collisional constitutive relations for granular materials, with application to plane shearing. *J Fluid Mech.* 1987;176:67–93.
98. Schneiderbauer S, Schellander D, Löderer A, Pirker S. Non-steady state boundary conditions for collisional granular flows at flat frictional moving walls. *Int J Multiphase Flow.* 2012;43:149–156.
99. Li T, Benyahia S. Revisiting Johnson and Jackson boundary conditions for granular flows. *AIChE J.* 2012;58:2058–2068.
100. Benyahia S, Syamlal M, Obrien T. Evaluation of boundary conditions used to model dilute, turbulent gas/solids flows in a pipe. *Powder Technol.* 2005;156:62–72.

101. Issangya AS, Grace JR, Bai D, Zhu J. Further measurements of flow dynamics in a high-density circulating fluidized bed riser. *Powder Technol.* 2000;111:104–113.
102. Manyele SV, Pärssinen JH, Zhu JX. Characterizing particle aggregates in a high-density and high-flux CFB riser. *Chem Eng J.* 2002; 88:151–161.
103. Gu WK, Chen JC. A model for solid concentration in circulating fluidized beds. In: Fan LS, Knowlton TM, editors. Fluidization IX. Durago, Colorado: Engineering Foundation, 1998:501–508.
104. Harris AT, Davidson JF, Thorpe RB. The prediction of particle cluster properties in the near wall region of a vertical riser (200157). *Powder Technol.* 2002;127:128–143.
105. van Buijtenen MS, van Dijk WJ, Deen NG, Kuipers JAM, Leadbeaterm T, Parker DJ. Numerical and experimental study on multiple-spout fluidized beds. *Chem Eng Sci.* 2011;66:2368–2376.
106. Chialvo S, Sun J, Sundaresan S. Bridging the rheology of granular flows in three regimes. *Phys Rev E.* 2012;85:021305.
107. Busciglio A, Vella G, Micale G, Rizzuti L. Analysis of the bubbling behaviour of 2D gas solid fluidized beds Part I. Digital image analysis technique. *Chem Eng J.* 2008;140:398–413.
108. Laverman JA, Roghair I, Van Sint Annaland M, Kuipers JAM. Investigation into the hydrodynamics of gas-solid fluidized beds using particle image velocimetry coupled with digital image analysis. *Can J Chem Eng.* 2008;86:523–535.
109. Werther J. Effect of gas distributor on the hydrodynamics of gas fluidized beds. *Ger Chem Eng.* 1978;1:166–174.
110. Mudde RF, Schulte HBM, van den Akker HEA. Analysis of a bubbling 2-d gas-fluidized bed using image processing. *Powder Technol.* 1994;81:149–159.
111. Hilligardt K, Werther J. Local bubble gas hold-up and expansion of gas/solid fluidized beds. *Ger Chem Eng.* 1986;9:215–221.
112. Botterill JSM, George JS, Besford H. Bubble chains in gas fluidized beds. *Chem Eng Prog Symp Ser.* 1966;62:7–14.
113. Kehoe PWK, Davidson JF. Continuously Slugging Fluidised Beds. *Inst Chem Eng Symp Ser.* 1971;33:97–116.
114. Milioli CC, Milioli FE, Holloway W, Agrawal K, Sundaresan S. Filtered two-fluid models of fluidized gas-particle flows: new constitutive relations. *AIChE J.* 2013, In press.
115. Srivastava A, Sundaresan S. Analysis of a frictional-kinetic model for gas-particle flow. *Powder Technol.* 2003;129:72–85.
116. Link J, Cuypers L, Deen NG, Kuipers JAM. Flow regimes in a spout-fluid bed: a combined experimental and simulation study. *Chem Eng Sci.* 2005;60:3425–3442.
117. Laverman JA. On the Hydrodynamics in Gas Polymerization Reactors. Enschede, Netherlands: Ipskamp Drukkers B. V, 2010.
118. Jenkins JT. Boundary conditions for rapid granular flows: flat, frictional walls. *J Appl Mech.* 1992;59:120–127.
119. Louge MY. Computer simulations of rapid granular flows of spheres interacting with a flat, frictional boundary. *Phys Fluids.* 1994;6:2253–2269.
120. Jenkins JT, Louge MY. On the flux of fluctuation energy in a collisional grain flow at a flat, frictional wall. *Phys Fluids.* 1997;9: 2835–2840.
121. Nasuno S, Kudrolli A, Bak A, Gollub JP. Time-resolved studies of stick-slip friction in sheared granular layers. *Phys Rev E.* 1998;58: 2161–2171.
122. Sommerfeld M, Huber N. Experimental analysis and modelling of particle-wall collisions. *Int J Multiphase Flow.* 1999;25:1457–1489.
123. Baldassarri A, Dalton F, Petri A, Zapperi S, Pontuale G, Pietronero L. Brownian forces in sheared granular matter. *Phys Rev Lett.* 2006;96:1–4.
124. Artoni R, Santomaso A, Canu P. Effective boundary conditions for dense granular flows. *Phys Rev E.* 2009;79:031304.

Appendix: *Two-fluid model equations*

In this article, we use the TFM approach for gas-particle flows presented in our previous studies.[23,42] The averaged continuity equation for phase q is written in Eq. 54. Note, Eqs. 54–70 are summarized in Table 3. In Eq. 54 $\boldsymbol{u}_q$ denotes the velocity, ϵ_q the volume fraction, and ρ_q the density of phase q. In the case of mono-dispersed gas-particle flows, q denotes either the gas phase g or the solid phase s. The averaged momentum equations for the gas–solid flow are given in Eqs. 55 and 56. It is well established that the interphase momentum exchange coefficient, that is, the drag coefficient β, of Wen and Yu[80] well predicts rising bubbles and bed expansion (Eq. 58). Even during the discharge of Geldart B particles from a hopper the interphase momentum exchange plays an important role.[115] In Eq. 58 d_s denotes the diameter of the spherical grains, μ_g the molecular viscosity of the gas phase, and Re_s the particle Reynolds number. However, (58) is only valid for homogeneously distributed particles, that is, subgrid effects such as clustering are negligible.

The stress-strain tensor for the gas phase, $\mathbf{T}_g$, in Eq. 60 is given by a simple Newtonian closure, where $\mathbf{D}_q$ denotes the rate-of-deformation tensor for phase q. In the literature, there is general agreement that the influence of gas turbulence on the gas stress tensor is negligible in the case of dense fluidized beds.[14,15,74,105,116,117]

While in dense particulate flows, the diffusive and convective transport of momentum is dominated by interparticle collisions and interparticle contacts (friction), in dilute particulate flows, it is determined by the translational motion of the grains. If a huge number of particles are involved, it will be practical to apply the kinetic theory of granular flows to close the solids stress tensor, $\mathbf{S}_s^{kc}$, arising from kinetic and collisional contributions. This closure requires, analogous to the kinetic theory of gases, that the above set of equations should be augmented by a balance of pseudothermal energy (PTE) of velocity fluctuations, E_{PTE}.[45] The balance equation for E_{PTE} is given by Eq. 57, where $\Theta=2/3E_{PTE}$ denotes the granular temperature. Finally, the kinetic and collisional solids stress tensor, $\mathbf{S}_s^{kc}$, is written in a compressible sense to account for the resistance of the granular particles to compression and expansion (Eq. 60). Here, p_s^{kc} denotes the solids pressure (Eq. 66), λ_s^{kc} the granular bulk viscosity (Eq. 66), and μ_s^{kc} the kinetic-collisional granular viscosity (Eq. 61).

In Eq. 57, the first term of the right hand side, $-\mathbf{S}_s^{kc}:\nabla\boldsymbol{u}_s$, determines the generation of PTE. The second term, $-\nabla\cdot$ q, represents the diffusion of PTE, where the flux vector $\boldsymbol{q}$ is defined in Eq. 63. The transfer of the kinetic energy of random fluctuations in particle velocity from the solids phase to the gas phase is represented by the third term, Γ_s, and forth term, J_v, on the right hand side of Eq. 57. The collisional dissipation, γ_Θ, represents the rate of dissipation of the PTE, Θ, due to inelastic collisions between particles determined by the restitution coefficient e_s (Eq. 64).

Equations 61 and 63 account for the role of the interstitial fluid by the terms μ^* and κ^*, respectively.[45] The radial distribution function g_0 has to be introduced to the collisional integral in the Boltzmann equation to incorporate the maximum packing limit, ϵ_s^{max}, to the kinetic theory of granular flows. We follow Schneiderbauer et al.,[23] who proposed Eq. 59 to comply $||\mathbf{S}^{fr}|| \gg ||\mathbf{S}^{kc}||$ in the frictional regime.

At high-volume fractions ($\epsilon_s \gtrsim 0.4$,[67]) grains start to endure long, sliding, and rubbing contacts, which gives rise to a totally different form of dissipation and stress, referred to as frictional contribution. We follow our previous study [23] and write the particulate stress tensor, $\mathbf{S}_s$, as the sum of kinetic, collisional ($\mathbf{S}_s^{kc}$) and frictional ($\mathbf{S}_s^{fr}$) contributions, that is,

$$\mathbf{S}_s=\mathbf{S}_s^{kc}+\mathbf{S}_s^{fr} \tag{53}$$

In the frictional regime at high-volume fraction the particle collisions are no longer instantaneous as assumed by kinetic theory. It is, therefore, concluded that an expression for the frictional part of the solids shear viscosity does not

Table 3. Model Equations for Gas-Particle Flows.[23]

Continuity equation, momentum equation and transport equation for PTE:

$$\frac{\partial}{\partial t}\epsilon_q\rho_q+\nabla\cdot\left(\epsilon_q\rho_q\boldsymbol{u}_q\right)=0 \tag{54}$$

$$\frac{\partial}{\partial t}\left(\epsilon_{\mathrm{g}}\rho_{\mathrm{g}}\boldsymbol{u}_{\mathrm{g}}\right)+\nabla\cdot\left(\epsilon_{\mathrm{g}}\rho_{\mathrm{g}}\boldsymbol{u}_{\mathrm{g}}\boldsymbol{u}_{\mathrm{g}}\right)=-\epsilon_{\mathrm{g}}\nabla p+\nabla\cdot\epsilon_{\mathrm{g}}\mathbf{T}_{\mathrm{g}}-\beta\left(\boldsymbol{u}_{\mathrm{g}}-\boldsymbol{u}_{\mathrm{s}}\right)+\epsilon_{\mathrm{g}}\rho_{\mathrm{g}}\boldsymbol{g} \tag{55}$$

$$\frac{\partial}{\partial t}\left(\epsilon_{\mathrm{s}}\rho_{\mathrm{s}}\boldsymbol{u}_{\mathrm{s}}\right)+\nabla\cdot\left(\epsilon_{\mathrm{s}}\rho_{\mathrm{s}}\boldsymbol{u}_{\mathrm{s}}\boldsymbol{u}_{\mathrm{s}}\right)=-\epsilon_{\mathrm{s}}\nabla p-\nabla\cdot\left(\mathbf{S}_{\mathrm{s}}^{\mathrm{kc}}+\mathbf{S}_{\mathrm{s}}^{\mathrm{fr}}\right)+\beta\left(\boldsymbol{u}_{\mathrm{g}}-\boldsymbol{u}_{\mathrm{s}}\right)+\epsilon_{\mathrm{s}}\rho_{\mathrm{s}}\boldsymbol{g} \tag{56}$$

$$\frac{3}{2}\left(\frac{\partial}{\partial t}\left(\epsilon_{\mathrm{s}}\rho_{\mathrm{s}}\Theta\right)+\nabla\cdot\left(\epsilon_{\mathrm{s}}\rho_{\mathrm{s}}\boldsymbol{u}_{\mathrm{s}}\Theta\right)\right)=-\mathbf{S}_{\mathrm{s}}^{\mathrm{kc}}:\nabla\boldsymbol{u}_{\mathrm{s}}-\nabla\cdot\boldsymbol{q}+\Gamma_{\mathrm{s}}-J_v-\gamma_{\Theta} \tag{57}$$

Drag law:

$$\beta_{\mathrm{WY}}=\frac{3}{4}C_{\mathrm{d}}\frac{\epsilon_{\mathrm{g}}\epsilon_{\mathrm{s}}\rho_{\mathrm{g}}\left\|\boldsymbol{u}_{\mathrm{g}}-\boldsymbol{u}_{\mathrm{s}}\right\|}{d_{\mathrm{s}}}\epsilon_{\mathrm{g}}^{-2.65},\qquad C_d=\begin{cases}\dfrac{24}{\mathrm{Re}_s}\left(1+0.15\mathrm{Re}_{\mathrm{s}}^{0.687}\right) & \mathrm{Re}_{\mathrm{s}}<10^3\\ 0.44 & \mathrm{Re}_{\mathrm{s}}\geq 10^3\end{cases},\qquad \mathrm{Re}_{\mathrm{s}}=\frac{\epsilon_{\mathrm{g}}\rho_{\mathrm{g}}\left\|\boldsymbol{u}_{\mathrm{g}}-\boldsymbol{u}_{\mathrm{s}}\right\|d_{\mathrm{s}}}{\mu_{\mathrm{g}}}. \tag{58}$$

Radial distribution function:

$$g_0=\min\left(\frac{1}{1-\epsilon_{\mathrm{s}}/\epsilon_{\mathrm{s}}^{\max}},\frac{1}{1-\epsilon_{\mathrm{s}}}+\frac{3}{2}\frac{\epsilon_{\mathrm{s}}}{\left(1-\epsilon_{\mathrm{s}}\right)^2}+\frac{1}{2}\frac{\epsilon_{\mathrm{s}}^2}{\left(1-\epsilon_{\mathrm{s}}\right)^3}\right) \tag{59}$$

Gas-phase and solids phase stress tensors:

$$\mathbf{T}_{\mathrm{g}}=2\mu_{\mathrm{g}}\mathbf{D}_{\mathrm{g}},\qquad \mathbf{S}_{\mathrm{s}}^{\mathrm{kc}}=\left(p_{\mathrm{s}}^{\mathrm{kc}}-\lambda_{\mathrm{s}}^{\mathrm{kc}}\,\mathrm{tr}\left(\mathbf{D}_{\mathrm{s}}\right)\right)\mathbf{I}-2\mu_{\mathrm{s}}^{\mathrm{kc}}\,\mathrm{dev}\,\mathbf{D}_{\mathrm{s}},\qquad \mathbf{S}_{\mathrm{s}}^{\mathrm{fr}}=p_{\mathrm{s}}^{\mathrm{fr}}\mathbf{I}-2\mu_{\mathrm{s}}^{\mathrm{fr}}\,\mathrm{dev}\,\mathbf{D}_{\mathrm{s}} \tag{60}$$

$$\mathbf{D}_{\mathrm{q}}=\tfrac{1}{2}\left(\nabla\boldsymbol{u}_{\mathrm{q}}+\left(\nabla\boldsymbol{u}_{\mathrm{q}}\right)^{\mathrm{T}}\right),\qquad \mathrm{dev}\,\mathbf{D}_s=\mathbf{D}_{\mathrm{s}}-\tfrac{1}{3}\mathrm{tr}\left(\mathbf{D}_s\right)\mathbf{I}$$

Solids viscosity:

$$\mu_{\mathrm{s}}^{\mathrm{kc}}=\left(\frac{2+a}{3}\right)\left\{\frac{\mu^*}{g_0\eta_s(2-\eta_s)}\left(\frac{1}{1+\frac{l_s}{\mathbb{L}}}+\frac{8}{5}\epsilon_{\mathrm{s}}\eta_{\mathrm{s}}g_0\right)\left(1+\frac{8}{5}\eta_{\mathrm{s}}(3\eta_{\mathrm{s}}-2)\epsilon_{\mathrm{s}}g_0\right)+\frac{3}{5}\eta_{\mathrm{s}}\mu_b\right\} \tag{61}$$

$$\mu^*=\frac{\mu}{1+\frac{2\beta\mu}{\left(\epsilon_{\mathrm{s}}\rho_{\mathrm{s}}\right)^2g_0\Theta}},\qquad \mu=\frac{5\rho_{\mathrm{s}}d_{\mathrm{s}}\sqrt{\pi\Theta}}{96},\qquad \mu_b=\frac{256\mu\epsilon_{\mathrm{s}}^2g_0}{5\pi},\qquad \alpha=\frac{8}{5},\qquad \eta_{\mathrm{s}}=\frac{1}{2}\left(1+e_{\mathrm{s}}\right) \tag{62}$$

PTE flux vector $\boldsymbol{q}$, rate of dissipation of PTE γ_{Θ}, rate of dissipation of PTE by viscous damping J_{v} and rate of production of PTE by gas-particle slip Γ_{s}:

$$\boldsymbol{q}=-\frac{\kappa^*}{g_0}\left\{\left(\frac{1}{1+\frac{l_{\mathrm{s}}}{\mathbb{L}}}+\frac{12}{5}\eta_{\mathrm{s}}\epsilon_{\mathrm{s}}g_0\right)\left(1+\frac{12}{5}\eta_{\mathrm{s}}^2(4\eta_{\mathrm{s}}-3)\epsilon_{\mathrm{s}}g_0\right)+\frac{64}{25\pi}(41-33\eta_{\mathrm{s}})\eta_{\mathrm{s}}^2\epsilon_{\mathrm{s}}^2g_0^2\right\}\nabla\Theta \tag{63}$$

$$\gamma_{\Theta}=\frac{48}{\sqrt{\pi}}\eta_{\mathrm{s}}(1-\eta_{\mathrm{s}})\frac{\rho_{\mathrm{s}}\epsilon_{\mathrm{s}}^2}{d_{\mathrm{s}}}g_0\Theta^{3/2},\qquad \kappa^*=\frac{\kappa}{1+\frac{6\beta\kappa}{5\left(\epsilon_{\mathrm{s}}\rho_{\mathrm{s}}\right)^2g_0\Theta}},\qquad \kappa=\frac{75\rho_{\mathrm{s}}d_{\mathrm{s}}\sqrt{\pi\Theta}}{48\eta_{\mathrm{s}}(41-33\eta_{\mathrm{s}})} \tag{64}$$

$$\Gamma_{\mathrm{s}}=\frac{81\epsilon_{\mathrm{s}}\mu_{\mathrm{g}}^2\left\|\boldsymbol{u}_g-\boldsymbol{u}_{\mathrm{s}}\right\|}{g_0d_{\mathrm{s}}^3\rho_{\mathrm{s}}\sqrt{\pi\Theta}},\qquad J_{\mathrm{v}}=3\beta\Theta \tag{65}$$

Solids pressure and bulk viscosity:

$$p_{\mathrm{s}}^{\mathrm{kc}}=\epsilon_{\mathrm{s}}\rho_{\mathrm{s}}\left(\frac{1}{1+\frac{l_s}{\mathbb{L}}}+4\eta_{\mathrm{s}}\epsilon_{\mathrm{s}}g_0\right)\Theta,\qquad \lambda_{\mathrm{s}}^{\mathrm{kc}}=\frac{8}{3}\eta_{\mathrm{s}}\epsilon_{\mathrm{s}}^2\rho_{\mathrm{s}}d_{\mathrm{s}}g_0\sqrt{\frac{\Theta}{\pi}} \tag{66}$$

Frictional pressure and viscosity:

$$p_{\mathrm{s}}^{\mathrm{fr}}=4\rho_{\mathrm{s}}\left(\frac{bd_{\mathrm{s}}\left\|\mathrm{dev}\,\mathbf{D}_{\mathrm{s}}\right\|}{\epsilon_{\mathrm{s}}^{\max}-\epsilon_{\mathrm{s}}}\right)^2 \tag{67}$$

$$\mu_{\mathrm{s}}^{\mathrm{fr}}\left(I_{\mathrm{s}},p_{\mathrm{s}}^{\mathrm{fr}},\mathrm{dev}\,\mathbf{D}_{\mathrm{s}}\right)=\frac{\mu_{\mathrm{i}}(I_{\mathrm{s}})p_{\mathrm{s}}^{\mathrm{fr}}}{2\left\|\mathrm{dev}\,\mathbf{D}_{\mathrm{s}}\right\|},\qquad \mu_{\mathrm{i}}(I_{\mathrm{s}})=\mu_{\mathrm{i}}^{\mathrm{st}}+\frac{\mu_{\mathrm{i}}^{\mathrm{c}}-\mu_{\mathrm{i}}^{\mathrm{st}}}{I_0/I_{\mathrm{s}}+1},\qquad I_{\mathrm{s}}=\frac{2\left\|\mathrm{dev}\,\mathbf{D}_{\mathrm{s}}\right\|d_{\mathrm{s}}}{\sqrt{p_{\mathrm{s}}^{\mathrm{fr}}/\rho_{\mathrm{s}}}}. \tag{68}$$

Table 4. Boundary Conditions for Gas-Particle Flows[23,98]

Boundary conditions for particulate phase in the collisional regime:

$$\boldsymbol{\tau}_{\mathrm{s}}^{\mathrm{kc}}=-\eta_{\mathrm{w}}\mu_{\mathrm{w}}\epsilon_s\rho_s g_0\Theta\mathrm{erf}\left(\overline{u}_s\right)\frac{\boldsymbol{u}_{\mathrm{s}}^{\mathrm{sl}}}{||\boldsymbol{u}_{\mathrm{s}}^{\mathrm{sl}}||},\qquad \mu_0=\frac{7}{2}\frac{1+e_{\mathrm{w}}}{1+\beta_0}\mu_{\mathrm{w}},\qquad \eta_{\mathrm{w}}=\frac{1}{2}(1+e_{\mathrm{w}})\qquad \overline{u}_s=\frac{||\boldsymbol{u}_s^{\mathrm{sl}}||}{\sqrt{2\Theta}\mu_0},\tag{69}$$

$$\begin{aligned}\boldsymbol{n}\cdot\boldsymbol{q}=\boldsymbol{\tau}_{\mathrm{s}}^{\mathrm{kc}}\cdot\boldsymbol{u}_{\mathrm{s}}^{\mathrm{sl}}-\frac{\epsilon_{\mathrm{s}}\rho_{\mathrm{s}}g_0\eta_{\mathrm{w}}\sqrt{\Theta}}{\sqrt{2}\mu_0^2\sqrt{\pi}}\exp\left(-\overline{u}_{\mathrm{s}}^2\right)\Big\{&\mu_{\mathrm{w}}\left[2\mu_{\mathrm{w}}||\boldsymbol{u}_{\mathrm{s}}^{\mathrm{sl}}||^2(2\eta_{\mathrm{w}}-\mu_0)+\Theta\left(14\mu_{\mathrm{w}}\eta_{\mathrm{w}}-4\mu_0(1+\mu_{\mathrm{w}})-6\mu_{\mathrm{w}}\mu_0^2\eta_{\mathrm{w}}\right)\right]\\&+\mu_0^2\sqrt{\Theta}\exp\left(\overline{u}_{\mathrm{s}}^2\right)\left[\sqrt{\Theta}\left(4(\eta_{\mathrm{w}}-1)+6\mu_{\mathrm{w}}^2\eta_{\mathrm{w}}\right)-\sqrt{2\pi}\mu_{\mathrm{w}}||\boldsymbol{u}_{\mathrm{s}}^{\mathrm{sl}}||\mathrm{erf}\left(\overline{u}_{\mathrm{s}}\right)\right]\Big\}\end{aligned}\tag{70}$$

Boundary conditions for particulate phase in the frictional regime:

$$\boldsymbol{\tau}_{\mathrm{s}}^{\mathrm{fr}}=-\frac{\boldsymbol{u}_{\mathrm{s}}^{\mathrm{sl}}}{||\boldsymbol{u}_{\mathrm{s}}^{\mathrm{sl}}||}\begin{cases}\tau_{\mathrm{s}}^{\mathrm{fr,ns}} & \tau_{\mathrm{s}}^{\mathrm{fr,ns}}<\tau_{\mathrm{s}}^{\mathrm{fr,sl}}\\ \tau_{\mathrm{s}}^{\mathrm{fr,sl}} & \text{else}\end{cases}\qquad\text{with}\qquad\begin{aligned}\tau_{\mathrm{s}}^{\mathrm{fr,sl}}&=\mu_{\mathrm{w}}||\boldsymbol{n}\cdot\mathbf{S}_{\mathrm{s}}^{\mathrm{fr}}\cdot\boldsymbol{n}||\\ \tau_{\mathrm{s}}^{\mathrm{fr,ns}}&=||\mathbf{S}_{\mathrm{s}}^{\mathrm{fr}}\cdot\boldsymbol{n}-\left(\boldsymbol{n}\cdot\mathbf{S}_{\mathrm{s}}^{\mathrm{fr}}\cdot\boldsymbol{n}\right)\boldsymbol{n}||\end{aligned}\tag{71}$$

depend on the amount of PTE. The frictional stress tensor is given by Eq. 60, where the frictional viscosity $\mu_{\mathrm{s}}^{\mathrm{fr}}$ is defined by Eq. 68. In our previous study,[23] it was shown that using a $\mu_i(I_s)$-rheology and a shear rate dependent frictional pressure $p_{\mathrm{s}}^{\mathrm{fr}}$ (Eqs. 67 and 68), which accounts for shear rate dependent dilation, delivers the correct dependence of the discharge rate on the particle diameter in the case of bin discharge. This is in contrast to state-of-the-art models such as the Princeton model.[115] Typical values for the constants in Eq. 68 obtained for mono-dispersed glass particles are $I_0=0.279$, $\mu_i^{\mathrm{st}}=\tan\left(20.9^{\circ}\right)$, and $\mu_i^{\mathrm{c}}=\tan\left(32.76^{\circ}\right)$.[64–67] Equation 68 states that in the quasi-static regime ($I_{\mathrm{s}}\lesssim 10^{-2}$) the effective friction coefficient, $\mu_i(I_{\mathrm{s}})$, is close to its minimum, μ_i^{st}. In the collisional regime ($I_{\mathrm{s}}\gtrsim 10^{-1}-10^{0}$) the friction coefficient saturates to μ_i^{c}. For mono-dispersed glass particles, the constants in Eq. 67 take the values $\epsilon_{\mathrm{s}}^{\max}\approx 0.6$ and $b\approx 0.2$.[67] Note that the frictional viscosity, $\mu_{\mathrm{s}}^{\mathrm{fr}}$, diverges as $\mathrm{dev}\,||\mathbf{D}_{\mathrm{s}}||$ tends to zero. This divergence ensures that a Drucker-Prager-like yield criterion exists. The frictional pressure diverges as well as the volume fraction tends to the volume fraction at maximum packing $\epsilon_{\mathrm{s}}^{\max}$. Both divergences can be treated numerically by regularization techniques.[23]

Following Schneiderbauer et al.[23,98] the wall shear stresses, $\boldsymbol{\tau}_{\mathrm{s}}^{\mathrm{kc}}$ and $\boldsymbol{\tau}_{\mathrm{s}}^{\mathrm{fr}}$, and the flux of fluctuation energy at the bounding walls, $\boldsymbol{n}\cdot\boldsymbol{q}$, are given in Table 4 by Eqs. 69–71. These boundary conditions incorporate sliding and nonsliding collisions.[118–124] e_{w} and β_0 denote the normal and tangential particle-wall restitution coefficients. μ_{w} is the coefficient of wall friction and $\boldsymbol{n}$ the outwarding surface unit normal. In Schneiderbauer et al.,[23] it was shown that these boundary conditions apply well to multiple-spout pseudo-2-D fluidized beds and moving beds.

Manuscript received Nov. 21, 2012, and revision received Mar. 6, 2013.